



Ferromagnetic resonance force spectroscopy of individual submicron-size samples

O. Klein,^{1,*} G. de Loubens,¹ V. V. Naletov,^{1,2} F. Boust,³ T. Guillet,¹ H. Hurdequint,⁴ A. Leksikov,¹ A. N. Slavin,⁵ V. S. Tiberkevich,⁵ and N. Vukadinovic⁶

¹*Service de Physique de l'État Condensé (CNRS URA 2464), CEA Saclay, 91191 Gif-sur-Yvette Cedex, France*

²*Physics Department, Kazan State University, Kazan 420008, Russia*

³*ONERA, 29 Avenue de la Division Leclerc, 92322 Châtillon Cedex, France*

⁴*Laboratoire de Physique des Solides, Université Paris-Sud, 91405 Orsay Cedex, France*

⁵*Department of Physics, Oakland University, Michigan 48309, USA*

⁶*Dassault Aviation, 78 quai Marcel Dassault, 92552 Saint-Cloud Cedex, France*

(Received 15 June 2008; revised manuscript received 9 September 2008; published 9 October 2008)

We review how a magnetic-resonance force microscope (MRFM) can be applied to perform ferromagnetic resonance spectroscopy of *individual* submicron-size samples. We restrict our attention to a thorough study of the spin-wave eigenmodes excited in Permalloy (Py) disks patterned out of the same 43.3-nm-thin film. The disks have a diameter of either 1.0 or 0.5 μm and are quasaturated by a perpendicularly applied magnetic field. It is shown that *quantitative* spectroscopic information can be extracted from the MRFM measurements. In particular, the data are extensively compared with complementary approximate models of the dynamical susceptibility: (i) a two-dimensional analytical model, which assumes a homogeneous magnetization dynamics along the thickness, and ii) a full three-dimensional micromagnetic simulation, which assumes a homogeneous magnetization dynamics below a characteristic length scale c and approximates the cylindrical sample volume by a discretized representation with regular cubic mesh of lateral size $c=3.9$ nm. In our analysis, the distortions due to a breaking of the axial symmetry are taken into account; both models incorporating the possibility of a small misalignment between the applied field and the normal of the disks.

DOI: [10.1103/PhysRevB.78.144410](https://doi.org/10.1103/PhysRevB.78.144410)

PACS number(s): 76.50.+g, 68.37.Rt, 75.30.Ds, 75.75.+a

I. INTRODUCTION

Development of innovative tools capable of measuring the local magnetization dynamics $\mathbf{M}(t, \mathbf{r})$ inside a ferromagnetic nanostructure is an objective of primary importance. New technology fields related to magnetic materials, such as spintronics, depend on one's ability to analyze and predict the out-of-equilibrium state of \mathbf{M} in nanoscale hybrid structures.

Several original techniques are being pursued to measure the dynamics of \mathbf{M} on small length scales. Among them, x-ray magnetic circular dichroism (XMCD) transmission microscopy,^{1,2} XMCD photoelectron microscopy (PEEM),³ microfocus Brillouin light scattering (BLS),⁴ time-resolved scanning Kerr microscopy (TRSKM),⁵⁻⁷ spin-torque driven ferromagnetic resonance (ST-FMR),⁸⁻¹⁰ and magnetic-resonance force microscopy (MRFM) applied to ferromagnetic resonance¹¹⁻¹⁵ are the most accomplished yet. This article focuses on the last one, called herein as mechanical-FMR, since a mechanical setup is used for the detection of ferromagnetic resonance (FMR), as shown in Fig. 1. Here, we shall review the ability of mechanical FMR to extract *quantitative* spectroscopic information in *individual* samples.

In FMR, the magnitude of the magnetization vector, $|\mathbf{M}(t, \mathbf{r})|=M_s$, is a constant of the motion and equals the saturation magnetization at the lattice temperature. Thus the dynamics of \mathbf{M} is governed by the position- and time-dependent transverse fluctuations of the magnetization direction, the so-called spin-waves (SW),¹⁶ $\mathbf{m}(t, \mathbf{r})=\mathbf{M}(t, \mathbf{r})-M_\zeta(\mathbf{r})\boldsymbol{\zeta}(\mathbf{r})$, where $M_\zeta=\mathbf{M}\cdot\boldsymbol{\zeta}$ is the longitudinal component of the magnetization defined as the projection of the instantaneous vector $\mathbf{M}(t)$ along the local precession axis of unit

vector $\boldsymbol{\zeta}(\mathbf{r})$. This equilibrium axis is parallel to the local effective magnetic field, $\mathbf{H}_{\text{eff}}=\partial_{\mathbf{M}}\mathcal{F}$, the conjugate variable of the magnetization, where \mathcal{F} is the free energy of the spin system and the shorthand notation $\partial_{\mathbf{M}}$ represents the derivative with respect to \mathbf{M} . Due to the exchange interaction, these transverse fluctuations are a collective precession and become more insightful once decomposed along the normal-mode basis of the sample. Therefore the experimental identification of this SW basis is important. Its nature depends primarily on the symmetry of the equilibrium configuration of \mathbf{M} inside the sample.¹⁷ In the case of a uniformly magnetized sample, the SW confinement is mostly governed by the shape of the sample. In thin films, the quantization of the

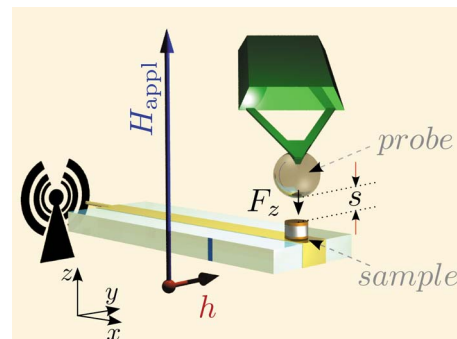


FIG. 1. (Color online) Schematic representation of the mechanical-FMR setup: the resonance spectra of a small size sample are detected by a magnetic force microscope. The probe consists here of a magnetic sphere glued at the extremity of the cantilever. The excitation comes from a microwave antenna placed underneath the sample.

lowest-energy (or longest-wavelength) modes develops along the finite-thickness direction, whereas in nanostructures, it arises both from the thickness and lateral confinements.

In a conventional-FMR experiment,¹⁸ the sample is placed in a region where a large homogeneous static magnetic field aligns the spins in a well-defined direction. On the emission side, a small microwave field h applied perpendicularly to \mathbf{H}_{eff} will cant the magnetization away from its equilibrium axis if the resonance condition is met, i.e., if the photon energy ($\hbar\omega_s$) corresponds to the energy to excite one SW or magnon. On the reception side, the measured quantity in a conventional spectrometer is $P_{\text{abs}} = \omega_s \chi'' h^2$, the microwave energy absorbed inside the sample per unit of time,^{19,20} which is proportional to χ'' , the dissipative part of the microwave transverse magnetic susceptibility.

The dependence of P_{abs} on either the applied magnetic field, H_{appl} , or the frequency of the excitation source, $\omega_s/2\pi$, reveals resonance peaks (bell-shaped curves). Their positions, amplitudes, and linewidths reflect the complete spectral information about the spin system. (i) The resonance condition depends on the spatial variation in the effective magnetic field $H_{\text{eff}}(\mathbf{r})$ along the mode profile. (ii) The amplitude is related to the coupling (overlap integral) with both the excitation and the detection schemes. It thus gives a hint about the spatiotemporal profile of the mode. For instance, with a cavity (cavity FMR) or a stripline antenna (stripline FMR), the microwave field h is uniform over the sample volume. As a result, it preferentially couples to the longest-wavelength SW modes of the sample. (iii) The *frequency* linewidth gives the decay rate of the excited SW (coherent with h) to the other degrees of freedom: the degenerate and thermal SW (incoherent with h) or the lattice (electrons and phonons). In FMR, the linewidth remains narrow despite the strong spatial inhomogeneity of $H_{\text{eff}}(\mathbf{r})$ inside the sample volume. This is a consequence of the nature of ferromagnetism, where the spins do not behave independently but are exchange coupled to one another. Experimentally, it is often easier to monitor the dependence of P_{abs} when H_{appl} is swept at fixed ω_s . In this case, it is crucial to repeat the measurement at several frequencies and to renormalize the *field* linewidth by the effective gyromagnetic ratio $\gamma_{\text{eff}} = \partial\omega_s / \partial H_{\text{appl}}$.

Although FMR is a sensitive technique (typical angles of precession are less than $\vartheta = 1^\circ$), the sensitivity of most conventional spectrometers is usually not sufficient to detect magnetization dynamics in individual submicron-size samples. The crucial parameter here is the ratio between the volume of the sample and the volume of the detector; the so-called filling factor. With the recent development of MRFM, the sensitivity of magnetic resonance has been tremendously enhanced. Nanometer scale sizes come now within reach as Rugar *et al.*²¹ at IBM Almaden recently showed with the detection of a single electron spin and with a record 90 nm resolution on nuclear paramagnets, where only a few thousands of nuclear spins contribute to the signal.²² The key to such performance comes from the size of the magnetic probe, which has a very strong coupling with the resonant volume, thus ensuring an almost optimized filling factor.

In this paper, we show how a mechanical-FMR setup can be used to perform FMR spectroscopy of submicron-size

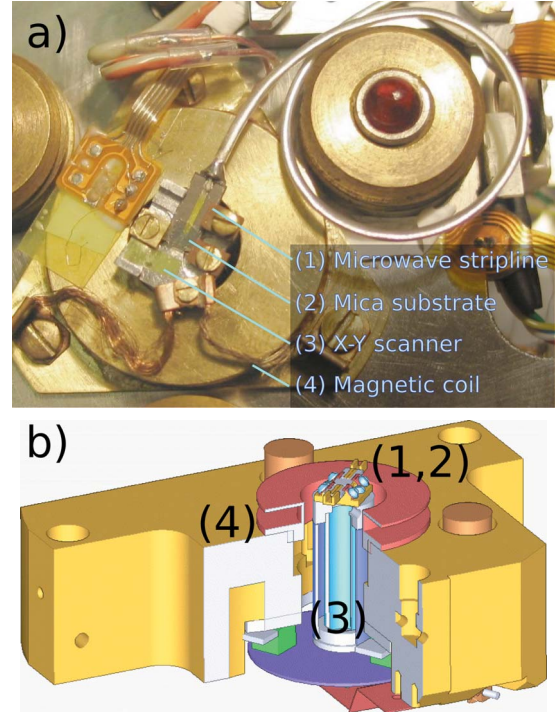


FIG. 2. (Color online) (a) Photograph of the MRFM bottom base showing (1) the microwave antenna, (2) the mica substrate where the Py disks are, (3) the piezoelectric scanner, and (4) the magnetic coil used for a calibrated modulation of the applied field. (b) Section view of the above elements. The top part with the cantilever and the optical detection is not shown.

samples. We present a thorough study of the SW eigenmodes in individual Permalloy (Py) disks, whose FMR spectra are compared to a two-dimensional (2D) approximate analytical model and to full three-dimensional (3D) micromagnetic simulations of the dynamical susceptibility. The structure of the rest of the paper is the following. Section II presents the principles of the mechanical-FMR and gives an extensive analysis of the spectral deformations induced by the magnetic probe on the measured FMR spectra. In Sec. III, the experimental results are presented. In Sec. IV, we derive an approximate 2D analytical model and present the results of a 3D micromagnetic simulation. They are both used in Sec. V to analyze the data. Sec. VI contains a summary of the results obtained.

II. MECHANICAL FMR

A. Experimental setup

The concept of mechanical detection of the magnetic resonance was first applied to FMR by Wigen and Hammel¹¹ in 1996. Figure 1 illustrates the mechanical-FMR setup, while Fig. 2 presents its experimental realization for the present study.

1. Excitation part

The sample magnetization is excited by a microstrip antenna placed underneath (see Figs. 1 and 2). The antenna

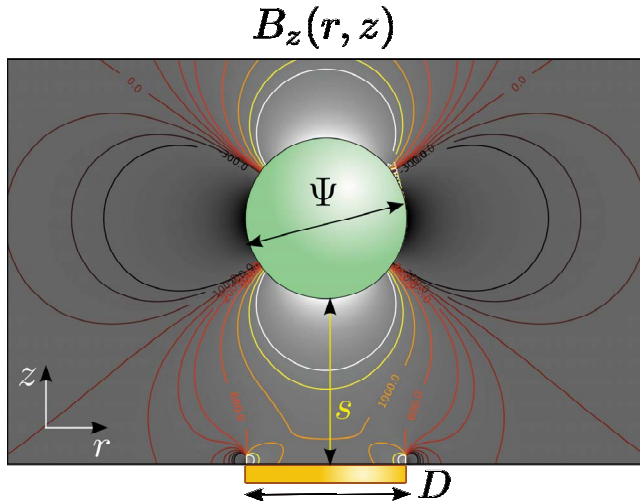


FIG. 3. (Color online) Visualization of the dipolar coupling interaction between a spherical magnetic probe (diameter Ψ) and a cylindrical Py disk (diameter D) separated by a distance s . The magnetic configurations in both objects are assumed to be saturated along z . The color lines represent the iso- B_z field lines. The bright and dark shades separate, respectively, the positive and negative coupling regions.

consists of a 1- μm -thick gold microstrip patterned by optical lithography on top of a sapphire substrate whose bottom surface is a Au ground plane. In order to obtain a wide-band antenna, the top Au electrode is shorted to the ground plane at the extremity of the substrate, hereby creating an antinode of microwave magnetic field at the extremity. Placing the submicron Py disks at this location ensures a wide-band excitation scheme (up to 20 GHz). The efficiency of this wide-band setup to induce large variation in the absorbed power depends (i) on the amplitude h of the excitation, (ii) on the volume of the sample, and (iii) on the susceptibility χ'' of the sample at resonance inversely proportional to the linewidth. It is important to keep the amplitude of h below saturation or other critical thresholds.²³ Indeed, significant spectral distortions are induced due to nonlinear effects. For these distortions being themselves a subject of research,²⁴ all the data shown hereafter are taken in the linear regime, where the peak amplitude remains proportional to the excitation power, i.e., precession angles limited to 1° .

2. Detection part

The detection scheme is directly inspired from magnetic force microscopy (MFM).

A soft cantilever with a magnetic tip is placed in the stray field of the sample to be studied. The dipolar coupling between the tip and the sample (see Fig. 3) creates a small flexion of the cantilever beam, which is detected optically by deflection of a laser beam on a four-quadrants photodiode. The pitch angle is produced by the vertical component of the force F_z (see Fig. 1) but also by the torque N_y , the component perpendicular to the beam axis and to the vertical direction. In all the experiments below, we will measure with a spherical probe the magnetization dynamics of disk-shaped Py samples perpendicularly magnetized by a homogeneous

applied field. H_{appl} is larger than the saturation field of Py, such that the magnetic state of the sample is almost uniform. In this situation, the coupling geometry preserves the axial symmetry; hence the mechanical coupling comes from the force F_z only ($N_y=0$).

There is a principal difference between the detected signal obtained by mechanical FMR and by conventional FMR. Mechanical FMR uses detectors which are only sensitive to M_z , the static (or longitudinal) component of the magnetization, i.e., to the susceptibility averaged on time scales which are much longer than any relaxation time in the spin system. The microwave oscillations of the transverse component do not couple to any mechanical mode of the cantilever, which typically oscillates in the audio range. When an FMR resonance is excited by the antenna, it is the deviation of M_z from M_s , $\Delta M_z = M_s - M_z$, that diminishes the force F_z on the cantilever (see Fig. 1). While conventional FMR measures the *absorbed* power (see above), mechanical FMR measures the *stored* energy.²⁵ The ratio between these two quantities is actually $1/T_1$, the relaxation rate of the out-of-equilibrium full magnons' population toward the lattice. The ΔM_z measurement is seldom obtained because this quantity is a second-order effect in the precession angle ϑ . $\Delta M_z/M_s = 1 - \cos \vartheta$ is thus much smaller than the transverse susceptibility, which is of first order in ϑ .

3. Imaging

Quite naturally, the scanning probe can be used here for imaging purpose. But the situation is different in paramagnetic²¹ and ferromagnetic spin systems. In a paramagnet, the spins are decoupled and the excitation is localized in a "resonant slice,"²⁶ whose thickness is inversely proportional to the field gradient produced by the magnetic tip. In contrast, neighboring spins in a ferromagnet are coupled through the exchange interaction and the spins precess collectively. An additional inhomogeneous field does not broaden the FMR linewidth but displace the resonance position. This effect can be exploited to increase the spatial resolution of mechanical FMR.¹⁴ The stray field of the magnetic tip can also alter the sample magnetic configuration just underneath the tip, leading to tip-induced FMR resonances. Hammel *et al.*²⁷ recently showed that it is possible to produce these new localized FMR modes by approaching the magnetic tip close to the sample surface. Exploitation of the spectral features of these new modes is still a challenge at the moment.

Detection wise, one benefits from the same advantage of an MFM. The spatial resolution is related to the size of the magnetic probe and the separation with the sample. In the present study, we are mostly interested by an optimization of the sensitivity of the mechanical detection, allowing us to measure smaller sample sizes. As will be shown below, optimization of the sensitivity requires us to choose a size of the magnetic probe of the order of the size of the sample (optimum filling factor²⁸). Furthermore, placing the probe far away from the sample surface and working in the weak-coupling regime diminishes the spectral alteration produced by the tip. Such conditions are quite obviously incompatible with good imaging conditions and an increase in the spatial

resolution (smaller probe) must then come at the detriment of the sensitivity.

B. Detection sensitivity

One of the main advantage of the mechanical FMR is its exquisite sensitivity. This is mainly due to the progress in nanofabrication technologies, which can produce micron-size mechanical structures with outstanding performance figures, i.e., achieving among the best compromise between small size and large quality factor.

1. Modulation technique

Exciting the sample at a fixed frequency ($\omega_s/2\pi$), spectroscopy is achieved by recording the cantilever motion as a function of the perpendicular dc applied field, H_{appl} , produced by an electromagnet. As mentioned before, the coupling between the mechanical oscillator and the microwave magnetization dynamics is purely static. However, it is possible and useful to modulate the microwave power at the mechanical resonance frequency of the first flexural mode of the cantilever, $f_c=3$ kHz in our case. As a result, the amplitude of vibration will be multiplied by Q , the quality factor of the mechanical resonator. Note that the mechanical noise is also amplified. However, a sensitivity gain is obtained if this intrinsic mechanical noise exceeds the preamplifier noise or the noise of the microwave source. This modulation technique is referred to as source or amplitude modulation. The amplitude of the microwave field follows the time dependence,

$$h(t) = he^{i\omega_s t} \left\{ \frac{1}{2} + \frac{1}{2} \cos(2\pi f_c t) \right\}, \quad (1)$$

where the depth of the modulation is 100%. Note that this modulation technique does not affect the line shape in the linear regime because the period of modulation $1/f_c$, is very large compared to the relaxation times T_1 and T_2 of the ferromagnetic system studied.

We mention that the modulation of the microwave field at f_c also induces a direct vibration of the cantilever even outside any resonance phenomena of the probe or of the sample. We attribute this to a modulation of the temperature of the cantilever. The latter is a direct consequence of the modulation of the microwave heating and eddy currents, mainly induced by e , the electric component of the electromagnetic radiation. This effect can distort the resonance peaks due to the modulation of the applied field on the sample by the vibrating magnetic probe. For instance, a sphere with a magnetic moment of 6×10^{-9} emu vibrating by 10 nm_{pp} induces a field modulation of about 6 Oe_{pp} on a sample placed at 2.7 μm from its center (separation $s=1.0$ μm , see below). This field modulation has no influence on the FMR signal if it is small compared to the linewidth but will otherwise significantly broaden the resonance. To eliminate it, a forced oscillation out of phase with the spurious contribution is produced by a piezoelectric bimorph slab placed nearby the cantilever. The resulting total vibration corresponds to a few nanometers at most. All the spectra shown below are ob-

tained in these conditions, where the amplitude of vibration of the cantilever is compensated so that it has no influence on the measured FMR spectra.

2. Minimal detectable force

In all MRFM setups, the detection noise is only limited by the Brownian motion of the cantilever, which behaves as a harmonic oscillator with a single degrees of freedom. Thus the minimal detectable force follows the relation

$$F_{\text{min}} = \sqrt{\frac{2k_B T k B}{\pi f_c Q}}, \quad (2)$$

where k is the spring constant of the cantilever, Q its quality factor, and B the detection bandwidth. Femto-Newton sensitive cantilevers are now readily available commercially. A BioLever B from Olympus with $k=5 \times 10^{-3}$ N/m has been used for this work. Because the cantilever is very sensitive to thermal fluctuations, it is important to stabilize both the intensity of the laser (to less than 15 ppm) that is shined on top of the cantilever for the position sensing but also the over-all temperature of the microscope (to less than 200 ppm) that is mounted on Peltier elements. To increase the sensitivity, the experiment is operated in a secondary vacuum of about 10^{-6} torr. Operating in vacuum is important to keep the large value of $Q=4500$. As seen in Eq. (2), the other parameters that control the minimum detectable force are the temperature and the bandwidth. Working at low temperature and averaging the signal over large period of time allows the detection of atto-Newton forces.²⁹ All the data shown hereafter are obtained at $T=280$ K and with a lock-in time constant of 1 s. From Eq. (2), the minimum detectable force [signal-to-noise ratio (SNR)=1] in our setup is 1 fN, the limiting noise being the thermal motion of the cantilever.

3. Magnetic spherical probe

Obviously the sensitivity directly depends on the strength of the dipolar coupling between the probe and the sample. As mentioned above, the magnetic probe must be carefully chosen because there is an optimal size for a given sample (concept of filling factor). In our case, the probe itself is a magnetic sphere glued at the apex of the cantilever. For a spherical probe, the static force applied on the cantilever is simply proportional to g_{zz} , the z component of the field gradient created by the sample at the center of the sphere,

$$F_z = m_{\text{sph}} g_{zz}, \quad (3)$$

where m_{sph} is the magnetic moment of the sphere. For a disk-shaped sample in contact, $s=0$, with the sphere, the largest force is obtained when the radius of the sphere $\Psi/2$ is equal to the diameter of the disk D ,³⁰ as shown in Fig. 4 (continuous line). The optimum point corresponds to the particular case where the sphere captures all the positive field lines emanating from the disk (see Fig. 3). The same figure also shows that the optimum Ψ increases if the separation between the two objects increases (dashed line).

A scanning electron microscopy (SEM) image of the sphere is shown in Fig. 5. Its diameter is $\Psi=3.5$ μm , which

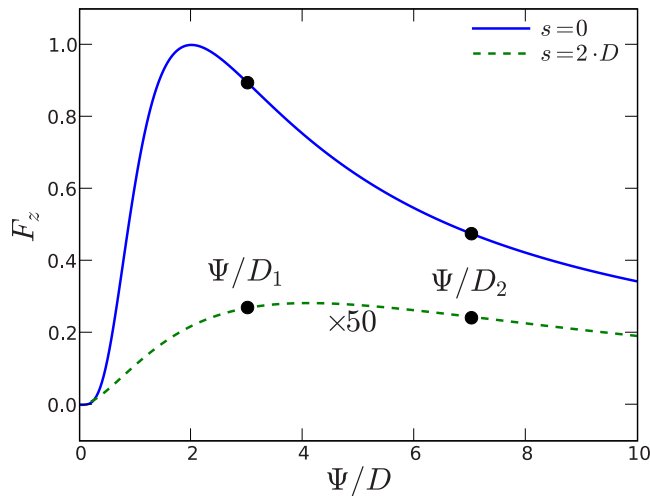


FIG. 4. (Color online) Variation in the dipolar magnetic force between a sphere and a disk as a function of the ratio between their diameters, respectively, Ψ and D . The continuous line shows the dependence when the two elements are brought into contact ($s=0$) and only Ψ is varied. The maximum force occurs when $\Psi=2D$. The dash line shows the behavior when the two elements are separated by $s=2D$ and only D is varied (close to the experimental conditions); the vertical scale has been multiplied by a factor of 50 for clarity purpose.

is slightly larger than the optimal size for our $D_1=1.0 \mu\text{m}$ and $D_2=0.5 \mu\text{m}$ sample diameters. This sphere is an amorphous alloy whose main constituents are Co (80 wt %), Fe (10 wt %), and Si (9 wt %), as deduced from chemical analysis. Its characteristics are measured after the gluing process of the sphere at the tip of the cantilever. The magnetization curve is obtained by placing the mounted cantilever above an Fe cylinder (diameter 2 mm and height 8 mm), which creates a well-characterized field gradient of $g_{zz}=0.5 \text{ G}/\mu\text{m}$. By monitoring the deformation of the cantilever vs the applied field, we can infer a 1.2 kG saturation field for the sphere. We also obtain the value of its magnetic mo-

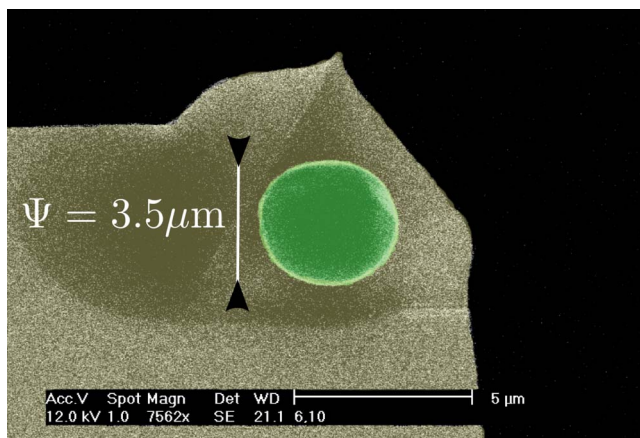


FIG. 5. (Color online) Scanning electron microscopy image of the CoFeSi magnetic sphere glued at the tip of an Olympus BioLever.

ment $m_{\text{sph}}=(6 \pm 0.5) \times 10^{-9} \text{ emu}$, which is deduced from the known values of the field gradient and the cantilever's spring constant.

We have already mentioned above the interest to preserve the axial symmetry, which is achieved if the center of the sphere is positioned above the center of the disk. Two other comments should be added about the choice of the spherical shape for the magnetic probe. First, in contrast to cylinders, spheres do not have any shape anisotropy. This property, combined with the absence of magnetocrystalline anisotropy of the amorphous alloy, considerably decreases the influence of the applied magnetic field on the mechanical resonance frequency of the cantilever. This is important because the source modulation technique relies on a phase-locked loop (PLL) to keep the source modulation exactly at the resonance frequency of the cantilever. Second, the magnetic probe on the cantilever is itself placed in the field gradient of the sample. As a result, mechanical vibrations of the cantilever are also produced by the excitation of the FMR modes of the probe itself. This can be seen as a reciprocal effect of the probe-sample coupling. Using different shapes for the probe (sphere) and for the sample (disk), the two FMR spectra are completely separated mainly due to the difference in the shape anisotropies of the two different geometries. In the spectral range shown in this study ($\omega_s/2\pi=4-10 \text{ GHz}$), the FMR resonance of the sphere occurs below 3 kOe,³¹ i.e., at much lower field than for the disks studied hereafter.

C. Extrinsic effects

1. Spectral deformations induced by the magnetic probe

The optimization of the sensitivity discussed above has, however, a drawback. Increasing the coupling between the probe and the sample inevitably produces a distortion of the spectral features. It is thus important to understand this effect and to keep it inside the perturbation regime so that one could still deduce the intrinsic behavior of the sample, i.e., without the presence of the probe. In mechanical FMR, the spectral distortions are due to the stray field of the probe. It produces an additional field inhomogeneity in the internal effective magnetic field, which affects the detailed SW dispersion relation inside the sample and thus the resonance condition. The strength of the effect depends on m_{sph} and on the separation s between the probe and the sample (see Figs. 1 and 3). We discuss in the following how to ensure that the field inhomogeneity produced by the probe is small compared to the internal dipolar field variations along the radial direction of the sample ($\approx 2\pi M_s$ for a nonellipsoidal shape).

Thorough experimental studies have been performed in the past on mechanical FMR of a $\text{Y}_3\text{Fe}_5\text{O}_{12}$ single-crystal disk for different separations s between the magnetic tip and sample surface.¹² It was found that when the bias field inhomogeneity from the probe is smaller than a few percents of the internal field variation inside the sample, its main effect is to shift the entire spectrum to higher frequency as s decreases. This shift is homogeneous within less than 10% for all the peaks corresponding to the different SW modes. In these conditions, their spatial profiles are almost not affected by the presence of the probe and the relative amplitudes be-

tween the peaks are kept to their intrinsic values. On the other hand, if the bias field from the tip represents a large perturbation to the internal field inside the isolated sample, the spatial profiles of the SW modes are affected^{31,32} and the observed FMR spectrum cannot be recognized as intrinsic to the sample. This situation can also lead to a different coupling between the probe and the sample.³¹ However, it is to note that since the mechanical probe is not coherent with the excitation, an increase in the coupling between the sample and the probe does not produce *any* additional contribution to the FMR linewidth.³³ This is in contrast to the radiation damping found when the coupling to the microwave resonator increases.²⁵

2. Quantitative analysis

A quantitative estimation of H_{off} , the shift induced by the tip on each SW mode, can be obtained analytically within a 2D model. By 2D, we mean here a model where the precessional profile of each mode in the disk only depends on the two in-plane coordinates, i.e., on (r, ϕ) in a cylindrical frame, and it is uniform along the thickness direction z . In that case, the resonance condition depends on the phase delay of the SW accumulated along the diameter. Constructive interferences occur when the phase delay over a cycle is equal to $n \times 2\pi$, where $n \in \mathbb{N}^*$. This condition is equivalent to the Wentzel-Kramers-Brillouin (WKB) approximation applied to the dispersion relation of magnetostatic forward volume waves (MSFVW) established by Damon and Eshbach³⁴ in 1961. In the following, we will use the dipole-exchange dispersion relation developed by Kalinikos and Slavin³⁵ for magnetized thin films and later applied by Kakazei *et al.*³⁶ for the case of disks magnetized in the exact perpendicular geometry.

We start with the normal-mode basis of a disk magnetized in the perpendicular direction, which are the $\mathcal{J}_m^\ell(\mathbf{r}) = J_\ell(k_{\ell,m}r)\cos(\ell\phi)$, where J_ℓ s are the Bessel functions of the first kind and $k_{\ell,m}$ is the modulus of the in-plane SW vector determined by the boundary conditions. We shall assume that the modes satisfy the dipolar pinning condition³⁷ at the circumference of the disk samples, i.e., $\mathcal{J}_m^\ell(\mathbf{R})=0$. Thus $k_{\ell,m} = \kappa_{\ell,m}/R$, where $\kappa_{\ell,m}$ is the $(m+1)$ th root of $J_\ell(x)$ and R is the radius of the disk. In this notation, ℓ and m are, respectively, the azimuthal and radial mode indices (i.e., the number of nodes in the circumferential and radial directions). Figure 6 is a color-coded representation of the transverse susceptibility χ'' corresponding to the first modes.

The obtention of an analytical formula for the resonance condition shall be detailed in Sec. IV A for the general case where the applied magnetic field makes a small angle θ_H with the normal of the disk [see Eqs. (29) and (30)]. For the estimation of the spectral deformations induced by the probe, we are only interested by the $\theta_H=0^\circ$ limit of the linearization of the equation of motion. The resonance condition for the normal mode (ℓ, m) in the perpendicular direction is given by the expression,³⁵

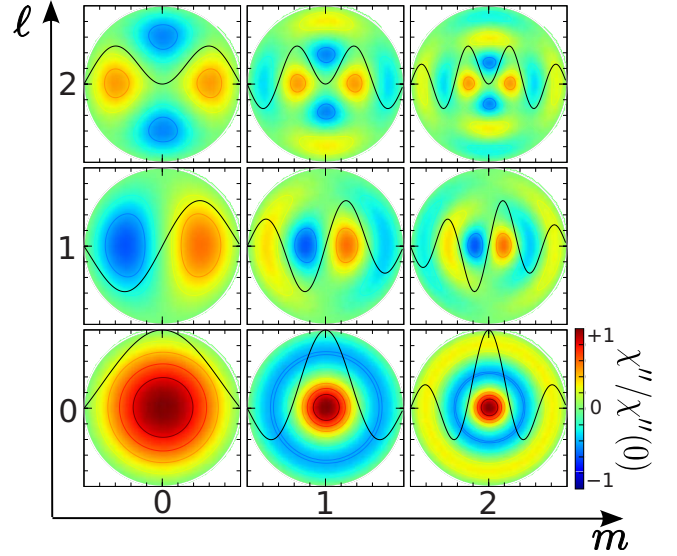


FIG. 6. (Color online) Color code representation of the eigenmodes basis $\mathcal{J}_m^\ell(\mathbf{r})$, where ℓ and m indicate, respectively, the number of nodes in the circumferential and radial direction. Only the modes $\ell=0$ couple to a uniform microwave excitation.

$$\omega_s = \sqrt{(\omega_{\text{int}} + \omega_M \Lambda^2 k_{\ell,m}^2)} \times \sqrt{\left[\omega_{\text{int}} + \omega_M \Lambda^2 k_{\ell,m}^2 + \left(\frac{1}{2} - G_{\ell,m}^\perp \right) \omega_M \right]}. \quad (4)$$

Here, $\omega_M = 4\pi\gamma M_s$ and $\omega_{\text{int}} = \gamma H_{\text{int}}$ is the mode-dependent averaged internal magnetic field,

$$H_{\text{int}} = H_{\text{ext}} - \widetilde{N}_{zz} 4\pi M_s + H_A, \quad (5)$$

where H_{ext} is the total external magnetic field, \widetilde{N}_{zz} is the longitudinal matrix element of the effective demagnetizing tensor [see Eq. (6)], and H_A is the perpendicular uniaxial anisotropy field (of spin-orbit coupling origin). $\Lambda = \sqrt{2A/(4\pi M_s^2)}$ is the exchange length, which depends on the exchange stiffness constant A expressed in erg/cm ($=10^{-6}$ in Py). Finally, the parameter $G_{\ell,m}^\perp$ is derived in Sec. IV A [Eq. (26)].

In our notation, \hat{N} is the demagnetizing tensor of the disk. Appendix A gives the analytical expression for the different matrix elements of this tensor in the cylindrical coordinates. In Eq. (5), the demagnetizing field along z depends on a matrix element of the effective demagnetization tensor $\hat{N}_{\ell,m}$. The latter is the demagnetizing tensor weighted by the spatial dependence of the normal-mode profile $\mathcal{J}_m^\ell(\mathbf{r})$,

$$\hat{N}_{\ell,m} = \frac{1}{C_{\ell,m}} \int_{r<R} \hat{N}(\mathbf{r}) \mathcal{J}_m^\ell(\mathbf{r})^2 d^2\mathbf{r}, \quad (6)$$

where $C_{\ell,m}$ is a renormalization constant,

$$C_{\ell,m} = \int_{r<R} \mathcal{J}_m^\ell(\mathbf{r})^2 d^2\mathbf{r}. \quad (7)$$

To calculate the influence of the sphere on the resonance field of the mode (ℓ, m) , we need to expand the external field

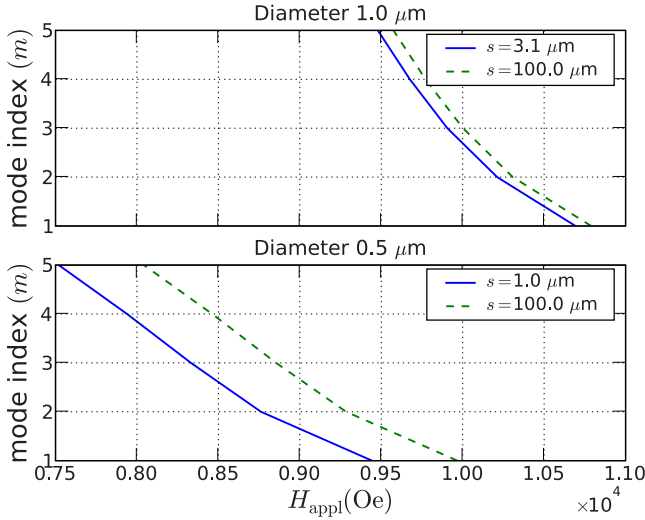


FIG. 7. (Color online) Calculated spectral deformation induced by the magnetic tip placed at distances $s=3.1$ and $1.0 \mu\text{m}$ above the disk samples $D_1=1.0 \mu\text{m}$ and $D_2=0.5 \mu\text{m}$, respectively. The graphs show the downward shift in field of each resonance mode (indexed by m) compared to the unperturbed FMR spectrum (dashed line).

as the sum of two contributions: the homogeneous magnetic field $H_{\text{appl}}\mathbf{z}$ produced by the electromagnet and the inhomogeneous stray field of the sphere $\mathbf{H}_{\text{sph}}(\mathbf{r})$;

$$\mathbf{H}_{\text{ext}}(\mathbf{r}) = \mathbf{H}_{\text{appl}} + \mathbf{H}_{\text{sph}}(\mathbf{r}). \quad (8)$$

Here we are only interested by its z component, $H_{\text{sph}}(\mathbf{r}) = \mathbf{H}_{\text{sph}}(\mathbf{r}) \cdot \mathbf{z}$. Then, the influence of the probe simply yields a modification of the internal magnetic field H_{int} of Eq. (5) by

$$H_{\text{int}} = H_{\text{appl}} + H_{\text{off}} - \widetilde{N}_{zz} 4\pi M_s + H_A, \quad (9)$$

where the shift H_{off} induced by the probe is averaged along the radial direction by the mode profile,

$$H_{\text{off}} = \frac{1}{C_{\ell,m}} \int_{r < R} H_{\text{sph}}(\mathbf{r}) \mathcal{J}_m^{\ell}(\mathbf{r})^2 d^2\mathbf{r}. \quad (10)$$

This expression allows us to give an estimation of the maximum coupling allowed to keep the spectral deformations in the perturbation regime. The additional contribution H_{off} must be small compared to the internal field variation inside the sample volume ($\sim \widetilde{N}_{zz} 4\pi M_s$) in order to keep the normal-mode basis unchanged. In the opposite case, the SW mode profiles and their resonance fields must be directly calculated from the MSFVW dispersion relation and from the magnetostatic potential. Clear experimental signatures of this strong influence of the probe on the SW mode can be found.³¹ The experiments presented below are not in this regime.

Quantitative results of the calculation are displayed in Fig. 7 for the two different disk diameters, $D_1=1.0 \mu\text{m}$ and $D_2=0.5 \mu\text{m}$. We have calculated the influence of the probe on the circumferentially symmetric ($\ell=0$) normal mode $\mathcal{J}_m^0(\mathbf{r})$. The values of M_s and γ used in the calculation are those derived below from cavity-FMR studies of the ex-

tended thin film. We also use the physical characteristics of the probe derived from the SEM images in Fig. 5 and magnetometry. The values of s (the separation between the sphere and the disk) used in Fig. 7 are close to the experimental conditions. The magnetic probe is brought closer to the disk surface as the sample diameter diminishes in an attempt to compensate for the reduction in the coupling strength. The induced force is expected to decrease by approximately an order of magnitude between the two disk diameters: a factor of 4 comes from the decrease in the resonating volume and a factor of 2 comes from the decrease in the filling factor. On the other hand, approaching the probe from $s=3.1 \mu\text{m}$ to $s=1.0 \mu\text{m}$ corresponds to an increase in the gradient by an order of magnitude (from $g_{zz}=6.1 \times 10^5$ to $5.8 \times 10^6 \text{ G/cm}$, respectively). Such compensation between these two effects is consistent with the calculation displayed in Fig. 4 where s is proportional to D . Figure 7 displays also as a reference the unperturbed case, i.e., the result obtained if the sphere is moved far away from the disk (the $s=100 \mu\text{m}$ calculation represented by the dashed line). Two important observations can be deduced from Fig. 7. First, the shift is almost independent of the mode number m . The spectral deformation can thus simply be modeled by an offset on the applied field. Second, at constant coupling, the amplitude of this offset increases when the disk diameter decreases, as the probe has to be brought closer to the smallest sample. In the case of our magnetic sphere, the displacement of the resonance field is about -100 Oe downward in field for the large disk and of -520 Oe for the small one.

In conclusion, under experimental conditions of an almost optimized coupling between the sample and the probe, the influence of the latter on the intrinsic FMR spectrum of the former is only an over-all downward shift in field, which can be quantitatively estimated. The fact that our sphere has a small moment and a large diameter keep the stray field homogeneous over the sample volume and reduces deformation in the relative position of the resonance modes. Assuming that the sphere is brought into contact with the surface of the disk, the variation in the perpendicular stray field along the radial direction of the disk is about 400 Oe , which is small compared to the $\widetilde{N}_{zz} 4\pi M_s \approx 10^4 \text{ Oe}$ variation in the internal field inside the disk.

III. SPECTROSCOPY OF SUBMICRON-SIZE DISKS

A. Film layered structure

Films corresponding to the composite system (Permalloy= $\text{Ni}_{80}\text{Fe}_{20}$, abbreviated by Py) have been deposited³⁸ by rf sputtering, at room temperature, on two different substrates: single crystalline Si and mica. A sweeping mode for sputtering has been used, where for each material the substrate-holder is swept back and forth over the activated target. Such a mode of deposition was chosen to achieve a better homogeneity of the magnetic layer and a good control of its thickness. Several multilayers $(\text{Py}|\text{Al}_2\text{O}_3)_N$ have been produced using this sweeping mode, being characterized by an individual layer in the ultrathin range. Low-angle x-ray diffraction measurements have been

performed on these multilayers (Si substrate) and the exploitation of these results has led to the determination of the deposition rates for the two materials. The specific magnetic film studied in the present report has the following layered structure: (Al_2O_3 base |Py| Al_2O_3 top). It consists of a single Py layer (43.3-nm thick) sandwiched by two Al_2O_3 layers of identical thickness (16 nm). The top alumina layer protects the Py layer from oxidation. The smooth amorphous Al_2O_3 base layer, characterized by a small surface roughness (a few angstroms) helps the growth of (111) textured Py polycrystalline layers in the low thickness range for the Py layers. The typical spread of surface orientation of the crystallites in the (111) textured Py layer grown by sputtering on the amorphous alumina is $\Delta\theta_H=0.5^\circ$. Due to the symmetry of the multilayer structure, the pinnings of the magnetization at the top and bottom (Py| Al_2O_3) interfaces are expected to be identical. Most importantly it is to be noted that in this layered structure the Py layer is sandwiched by an insulator. Consequently, by contrast to the case^{39,40} of an adjacent metallic layer (Py| N), where N designates a normal metal, no modification of the Py intrinsic damping (a spin-diffusion phenomena) is expected to arise from the (Py| Al_2O_3) interfaces.

B. Cavity-FMR studies of the extended thin films

Cavity-FMR experiments have been performed on the extended thin films deposited on Si and mica, corresponding to the layered structure described above ($16\text{Al}_2\text{O}_3|43.3\text{Py}|16\text{Al}_2\text{O}_3$), with individual thickness in nanometer. The basic FMR experiment which has been carried out (reflection at X-band, 9.6 GHz, and room temperature) consists in studying the resonance spectrum as a function of the orientation $\theta_H=(z, \mathbf{H}_{\text{appl}})$ of the dc field \mathbf{H}_{appl} applied in a plane perpendicular to the film. The resonance condition³⁸ for the uniform mode, as a function of θ_H , depends only on two parameters: the gyromagnetic ratio γ and the total perpendicular anisotropy field, $H_u=4\pi M_s-H_A$. The two fitting parameters (γ, H_u) are deduced from the observed angular variation in the resonance field. Very close values of these two parameters are found for the films grown on Si and on mica. For the film grown on mica, used to pattern the submicron disks, the gyromagnetic ratio is $\gamma=1.849 \times 10^7 \text{ rad s}^{-1} \text{ Oe}^{-1}$, corresponding to a Landé factor $g=2.103 \pm 0.004$. The perpendicular anisotropy field $H_u=9775 \pm 50 \text{ Oe}$ reflects entirely the demagnetizing field $4\pi M_s$ and corresponds to the expected value of the magnetization for a NiFe alloy of atomic composition $\text{Ni}_{80}\text{Fe}_{20}$. In fact, the spin-orbit anisotropy field H_A that is ascribed³⁸ to a stress-induced anisotropy observed in the ultrathin NiFe layers is here, for this thick Py layer, nearly zero (at least $<100 \text{ Oe}$) due to the fact that for this alloy composition the magnetostriction reduces nearly to zero. We mention also that this thick Py layer is characterized by a small uniaxial in-plane anisotropy, which is identified to a field-induced anisotropy built during the film deposition. Its small value, $7.5 \pm 0.5 \text{ Oe}$, is deduced from the two parallel geometry FMR measurements with the magnetic field applied, respectively, along the easy and the hard in-plane axis.

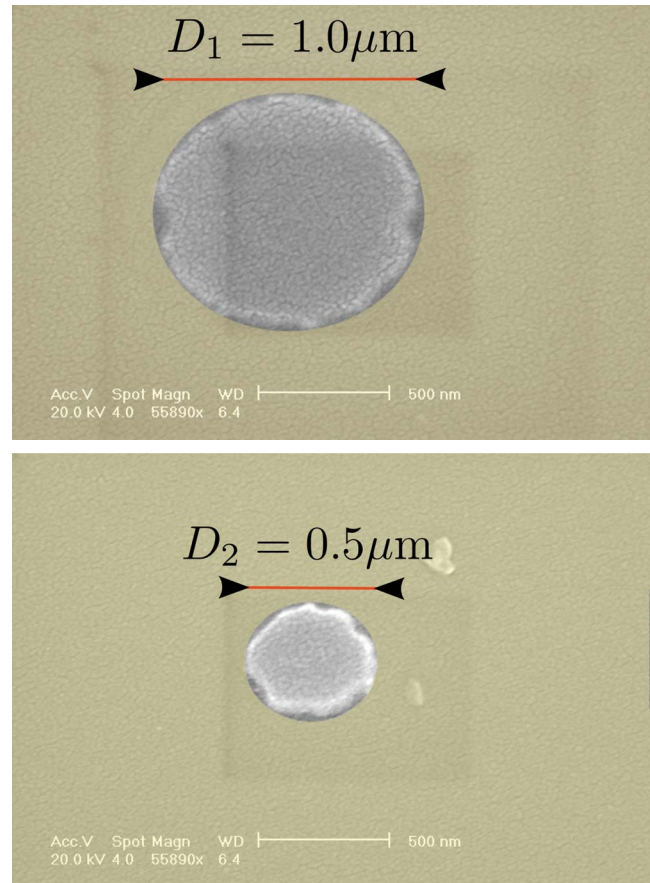


FIG. 8. (Color online) SEM images of the two Py disks samples. The images are being viewed at an angle of about 15° with respect to the normal of the substrate, thus distortions exist in the vertical direction.

C. Mechanical-FMR studies of the patterned structures

The disks prepared for the mechanical-FMR experiment were patterned out from the ($\text{Al}_2\text{O}_3|\text{Py}|\text{Al}_2\text{O}_3$) film grown on mica. Because this substrate cleaves easily, it was possible to reduce its thickness down to about $15 \mu\text{m}$ before gluing it on the broadband stripline. As a result from the short distance between the sample and the excitation circuit, the ac field h at the sample location can be achieved up to 10 Oe for the available power from the synthesizer. However, in the results presented below, h was restricted to 1 Oe in order to avoid nonlinear effects. The mechanical-FMR data are all collected at $T=280 \text{ K}$. The microscope was aligned so that the normal of the mica substrate was lying within 5° with the dc field.

The disks studied below have been patterned out of the same thin film deposited on mica which was studied by cavity-FMR. An aluminum mask defined by electron-beam (e -beam) lithography is used to protect the Py disks during the subsequent ion etching of the thin magnetic film. Several disks of nominal diameters 0.5 and $1.0 \mu\text{m}$ separated from each other by $50 \mu\text{m}$ were defined using this lithographic process. Figure 8 shows SEM images of two such patterned disks. They do not correspond to the measured disks, whose FMR spectra are presented in Figs. 9 and 10, but were pro-

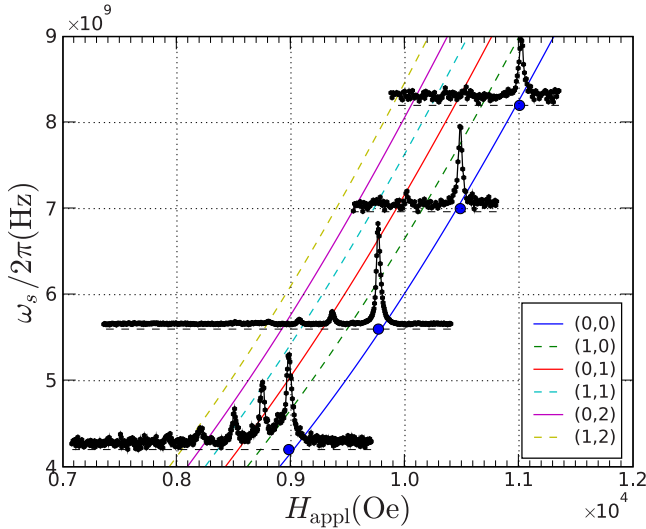


FIG. 9. (Color online) Mechanical-FMR spectra of the $D_1 = 1.0 \mu\text{m}$ disk measured at 4.2, 5.6, 7.0, and 8.2 GHz and $s \approx 3.1 \mu\text{m}$. The blue circles indicate the positions of the most intense peak. The lines are the analytical predictions of the locus of the (ℓ, m) modes when $\theta_H = 4.9^\circ$ and $H_{\text{off}} = -70 \text{ Oe}$.

cessed using the same recipe. A thin Au layer had to be deposited before the SEM imaging to avoid charging too much the mica substrate. The shape and the dimensions of the samples are as expected (the slightly elliptical shape seen on the images is due to perspective). The edge roughness, which is about 30 nm, could be due to uncertainties in the lithographic process on mica, an insulating substrate. It is not expected to influence too much the eigenmodes profiles of a perfect disk (presented in Fig. 6) and their resonance fields as their amplitude vanish at the periphery of the disk. These radial fluctuations do not either contribute to the FMR linewidth when the measurement is made with the field parallel

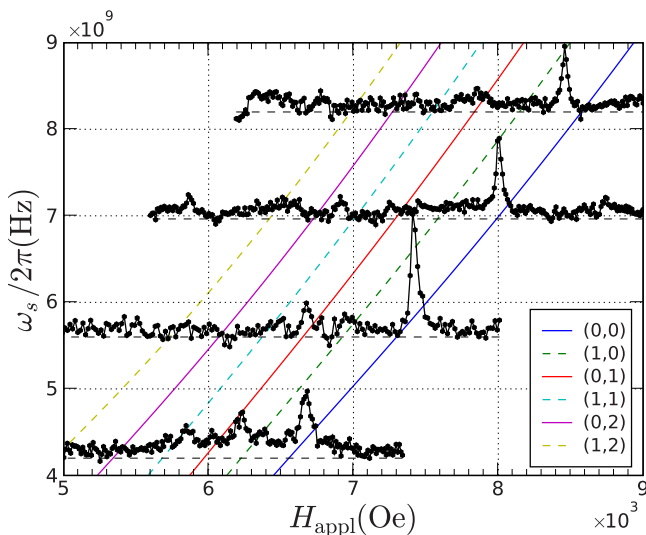


FIG. 10. (Color online) Mechanical-FMR spectra of the $D_2 = 0.5 \mu\text{m}$ disk measured at 4.2, 5.6, 7.0, and 8.2 GHz and $s \approx 1.0 \mu\text{m}$. The lines are the analytical predictions of the locus of the (ℓ, m) modes when $\theta_H = 9.5^\circ$ and $H_{\text{off}} = -760 \text{ Oe}$.

to the normal of the disk. In that case, only inhomogeneities along the thickness (i.e., the magnetization direction) have a direct impact on the linewidth broadening.¹⁸

1. Mechanical-FMR study of the $D_1 = 1.0 \mu\text{m}$ disk

The mechanical-FMR measurement on the $D_1 = 1.0 \mu\text{m}$ disk was performed with a probe-sample separation $s \approx 3.1 \mu\text{m}$, kept constant at the four different frequencies studied and shown in Fig. 9. To ensure that the separation is the same between the different spectra, a fine tuning of s is operated at the beginning of each scan (same H_{appl}) so as to keep the frequency of the cantilever identical. A series of magnetostatic modes is observed at each microwave frequency, with the most intense at the highest field, i.e., at the lowest energy. It corresponds to the mode whose coupling with the excitation is at maximum because it is the longest-wavelength mode. We note that the 5.6 GHz spectrum has been measured for a larger integration time than the other spectra, which explains its better signal-to-noise ratio and allows one to clearly observe the small amplitude low-field modes. The detailed analysis of the spectral features (position, amplitude, and linewidth) of the $D_1 = 1.0 \mu\text{m}$ disk is done in Sec. V, based on the models developed in Sec. IV.

2. Mechanical-FMR study of the $D_2 = 0.5 \mu\text{m}$ disk

The mechanical-FMR study on the $D_2 = 0.5 \mu\text{m}$ disk was performed with a probe-sample separation $s \approx 1.0 \mu\text{m}$, kept constant at the four different frequencies studied and shown in Fig. 10. As for the $D_1 = 1.0 \mu\text{m}$ disk, different magnetostatic modes can be observed, with the most intense at high field. The main difference with the larger disk is that this largest peak happens at much lower field ($\approx 2.5 \text{ kOe}$ less). It cannot be explained solely by the larger stray field from the probe, which is closer from the sample. Actually, most of this shift is due to finite-size effects. The latter are also responsible for the larger separation between modes on the smaller disk.¹³ A detailed analysis of the spectral features (position, amplitude, and linewidth) of this disk is done in Sec. V.

We note in passing that the SNR obtained at $T = 280 \text{ K}$ with a time constant of 1 s on this tiny sample is about 10 for a precession angle $\vartheta_m \approx 0.3^\circ$ [see Eq. (32)]. This translates in a spin sensitivity (SNR=1) of about 1000 spins for our mechanical-FMR setup. We also recall that sensitivity can be increased further by increasing the field gradient produced by the cantilever.

IV. MODELING OF THE SPECTRA

We shall present below two different approaches to analyze the experimental data. The first one is a 2D approximate analytical model, which assumes an homogeneous magnetization dynamics along the thickness. The second one is a full 3D micromagnetic simulation of the dynamical susceptibility using a discretized representation of the $0.5 \mu\text{m}$ disk with regular cubic cells of 3.9 nm lateral size and assuming an homogeneous magnetization dynamics inside each cell.

The motivation is to develop a comprehensive framework to analyze the spectroscopic features observed experimen-

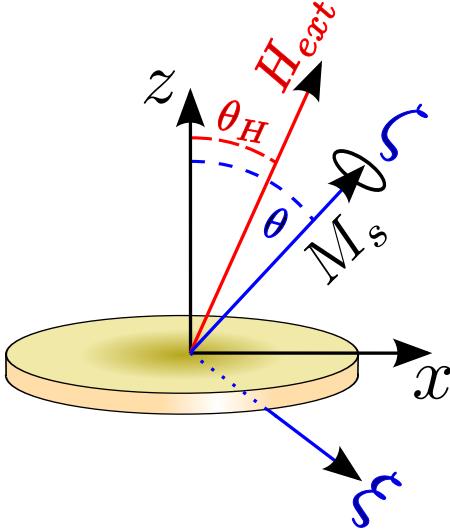


FIG. 11. (Color online) Graphic representation of the Cartesian frame (ξ, ζ) (blue) rotated in the direction of the equilibrium magnetization when the applied field makes an angle θ_H with the normal of the disk (z axis).

tally by mechanical FMR. Most parameters of the models are evaluated independently. The magnetic parameters of our Py are extracted from cavity FMR of the reference film. The diameters and thickness of the disks are cross-checked by AFM microscopy. A small misalignment $\theta_H \neq 0^\circ$ between the applied dc field and the normal of the disks is used to fit the mechanical-FMR data. To predict the effects of this misalignment, we shall use a perturbation approach, assuming that the profile of the modes is unchanged compared to the perfect perpendicular alignment. By comparing the analytical models and the simulations, we will evaluate the range of validity of this approximation.

A. 2D analytical model

In this section, we derive analytically the resonance condition that applies to the case where the external magnetic field makes a small angle θ_H with the normal of the disk, which breaks the axial symmetry. The notations used below are defined in Fig. 11.

The idea is to perform a linearization of the equation of motion for the magnetization around the equilibrium configuration using the SW dispersion relation in the dipole-exchange regime. We start with the local gyromagnetic term of the Landau-Lifshitz equation of motion for the magnetization,

$$\partial_t \mathbf{M} = \gamma [\mathbf{H}_{\text{eff}} \times \mathbf{M}]. \quad (11)$$

The effective magnetic field,

$$\mathbf{H}_{\text{eff}} = \mathbf{H}_{\text{ext}} + \mathbf{H}_{\text{ex}} + \mathbf{H}_{\text{dip}}, \quad (12)$$

is the sum of three fields: (i) \mathbf{H}_{ext} , the external magnetic field, which includes the stray field produced by the probe, (ii) the exchange field,

$$\mathbf{H}_{\text{ex}} = 4\pi\Lambda^2 \nabla^2 \mathbf{M}, \quad (13)$$

with Λ being the exchange length, and (iii) \mathbf{H}_{dip} the internal dipolar field of the sample,

$$\mathbf{H}_{\text{dip}}(t, \mathbf{r}) = -4\pi \int_{r' < R} \hat{\mathbf{G}}(\mathbf{r} - \mathbf{r}') \cdot \mathbf{M}(t, \mathbf{r}') d^2 \mathbf{r}'. \quad (14)$$

Here R is the radius of the disk and $\hat{\mathbf{G}}(\mathbf{r})$ is the dipolar Green's tensor that has the form,

$$\hat{\mathbf{G}}(\mathbf{r}) = \int \hat{\mathbf{G}}_k e^{i\mathbf{k} \cdot \mathbf{r}} \frac{d^2 \mathbf{k}}{(2\pi)^2}, \quad (15)$$

which introduces nonlocal interactions. The Fourier image $\hat{\mathbf{G}}_k$ of the dipolar Green's tensor for the lowest SW branch (with uniform magnetization across the film thickness) is given by³⁵

$$\hat{\mathbf{G}}_k = P_k \mathbf{z}\mathbf{z} + (1 - P_k) \frac{\mathbf{k}\mathbf{k}}{k^2}, \quad (16)$$

where

$$P_k = \frac{1 - e^{-kt}}{kt}, \quad (17)$$

\mathbf{z} is the unit vector orthogonal to the disk plane, t is the thickness of the ferromagnetic film, and \mathbf{k} the SW vector.

We shall derive below the collective equation of motion averaged over the sample volume. For a *thin* magnetic disk (with aspect ratio $t/R \ll 1$) we can neglect nonuniformities of the equilibrium magnetization distribution $\mathbf{M}(\mathbf{r})$. It will be assumed that $\mathbf{M}(\mathbf{r}) = M_s \hat{\boldsymbol{\zeta}}$, where $\hat{\boldsymbol{\zeta}}$ is a constant unit vector along the effective magnetic-field direction (not necessarily aligned with \mathbf{z}). At equilibrium, a uniform magnetization will create a nonuniform dipolar field $-4\pi M_s \hat{\mathbf{N}} \cdot \hat{\boldsymbol{\zeta}}$, where $\hat{\mathbf{N}}$ is the position-dependent static demagnetization tensor defined in Appendix A. The unit vector $\hat{\boldsymbol{\zeta}}$ is determined by the condition,

$$(\mathbf{H}_{\text{ext}} - 4\pi M_s \hat{\mathbf{N}} \cdot \hat{\boldsymbol{\zeta}}) \parallel \hat{\boldsymbol{\zeta}}. \quad (18)$$

This can be rewritten as

$$H_{\text{ext}} \sin(\theta - \theta_H) + 2\pi M_s \overline{N_{xx}} \sin 2\theta - 2\pi M_s \overline{N_{zz}} \sin 2\theta = 0, \quad (19)$$

allowing one to determine the equilibrium angle of the magnetization with respect to the normal of the disk. $\hat{\mathbf{N}}$ is the averaged demagnetization tensor over the volume of the disk,

$$\hat{\mathbf{N}} = \frac{1}{\pi R^2} \int_{r < R} \hat{\mathbf{N}}(\mathbf{r}) d^2 \mathbf{r}. \quad (20)$$

For small perturbations around the equilibrium state, the transverse part of the magnetization $\mathbf{m}(t, \mathbf{r}) = \mathbf{M}(t, \mathbf{r}) - M_s \hat{\boldsymbol{\zeta}}$ obeys the linear equation,

$$\begin{aligned} \partial_t \mathbf{m} = & \gamma [(\mathbf{H}_{\text{ext}} - 4\pi M_s \hat{\mathbf{N}} \cdot \boldsymbol{\zeta}) \times \mathbf{m}] \\ & + \gamma M_s [(\mathbf{h}_{\text{dip}} + 4\pi \Lambda^2 \nabla^2 \mathbf{m}) \times \boldsymbol{\zeta}], \end{aligned} \quad (21)$$

where

$$\mathbf{h}_{\text{dip}}(t, \mathbf{r}) = -4\pi \int_{r' < R} \hat{\mathbf{G}}(\mathbf{r} - \mathbf{r}') \cdot \mathbf{m}(t, \mathbf{r}') d^2 \mathbf{r}'. \quad (22)$$

We recall that for axially symmetric samples with negligible thickness, the normal modes are of the form

$$\mathbf{m}_{\ell, m}(t, \mathbf{r}) = \mathcal{J}_m^\ell(\mathbf{r}) \boldsymbol{\mu}_{\ell, m}(t) = J_\ell(k_{\ell, m} r) \cos(\ell \phi) \boldsymbol{\mu}_{\ell, m}(t), \quad (23)$$

where $\boldsymbol{\mu}_{\ell, m}$ is a left circularly polarized unit vector rotating at ω_s , ℓ and m are, respectively, the azimuthal and radial mode indices, $J_\ell(x)$ are Bessel functions, and the wave numbers $k_{\ell, m}$ are determined by the boundary conditions.

For a thin disk one can assume that the mode profiles remain the same as in the limit $t \rightarrow 0$. Substituting Eq. (23) into Eq. (21), multiplying by $J_\ell(k_{\ell, m} r) \cos(\ell \phi)$, and averaging over the disk area, one obtains the usual differential equation for the unit vector $\boldsymbol{\mu}_{\ell, m}$,

$$\begin{aligned} \partial_t \boldsymbol{\mu}_{\ell, m} = & \gamma [(\mathbf{H}_{\text{ext}} - 4\pi M_s \hat{\mathbf{N}}_{\ell, m} \cdot \boldsymbol{\zeta}) \times \boldsymbol{\mu}_{\ell, m}] \\ & - 4\pi \gamma M_s \{ [\hat{\mathbf{G}}_{\ell, m} \cdot \boldsymbol{\mu}_{\ell, m} + (\Lambda k_{\ell, m})^2 \boldsymbol{\mu}_{\ell, m}] \times \boldsymbol{\zeta} \}. \end{aligned} \quad (24)$$

where $\hat{\mathbf{N}}_{\ell, m}$ has been defined in Eq. (6).

The tensor $\hat{\mathbf{G}}_{\ell, m}$ is equal to

$$\begin{aligned} \hat{\mathbf{G}}_{\ell, m} = & \frac{1}{C_{\ell, m}} \int_{r < R} \int_{r' < R} \hat{\mathbf{G}}(\mathbf{r} - \mathbf{r}') J_\ell(k_{\ell, m} r) J_\ell(k_{\ell, m} r') \\ & \times e^{i\ell(\phi' - \phi)} d^2 \mathbf{r}' d^2 \mathbf{r} \\ = & G_{\ell, m}^\perp \mathbf{z}\mathbf{z} + (1 - G_{\ell, m}^\perp) (\mathbf{x}\mathbf{x}), \end{aligned} \quad (25)$$

where

$$\begin{aligned} G_{\ell, m}^\perp = & \frac{2\pi R^2}{C_{\ell, m}} \\ & \times \int_0^\infty \left(\frac{k J_{\ell-1}(kR) J_\ell(k_{\ell, m} R) - k_{\ell, m} J_{\ell-1}(k_{\ell, m} R) J_\ell(kR)}{k^2 - k_{\ell, m}^2} \right)^2 \\ & \times P_k k dk. \end{aligned} \quad (26)$$

P_k has been defined in Eq. (17) and the expression for the normalization constant $C_{\ell, m}$ is given in Eq. (7) and simplifies to

$$C_{\ell, m} = \pi R^2 [J_{\ell+1}(k_{\ell, m} R) J_{\ell-1}(k_{\ell, m} R)]. \quad (27)$$

Equation (24) is a system of ordinary differential equations with constant coefficients. The tensors $\hat{\mathbf{N}}_{\ell, m}$ and $\hat{\mathbf{G}}_{\ell, m}$ are given by one-dimensional integrals and are computed numerically. The resonance field is obtained by solving Eq. (24) (see Appendix B). It yields

$$\partial_t m_x = -\omega_1 m_y \quad (28a)$$

and

$$\partial_t m_y = +\omega_2 m_x, \quad (28b)$$

where

$$\begin{aligned} \frac{\omega_1}{\gamma} = & H_{\text{ext}} \cos(\theta - \theta_H) \\ & + 2\pi M_s [-\widetilde{N}_{zz} - \widetilde{N}_{xx} - (+\widetilde{N}_{zz} - \widetilde{N}_{xx}) \cos(2\theta)] \\ & + 4\pi M_s \Lambda^2 k_{\ell, m}^2 \end{aligned} \quad (29a)$$

$$\begin{aligned} \frac{\omega_2}{\gamma} = & H_{\text{ext}} \cos(\theta - \theta_H) \\ & + 2\pi M_s [-\widetilde{N}_{zz} - \widetilde{N}_{xx} - (+\widetilde{N}_{zz} - \widetilde{N}_{xx}) \cos(2\theta)] \\ & + 4\pi M_s \Lambda^2 k_{\ell, m}^2 + 2\pi M_s (1 - 2G_{\ell, m}^\perp) \cos(2\theta). \end{aligned} \quad (29b)$$

This system of homogeneous equation has periodic solutions if the determinant of the characteristic system is equal to zero. This leads finally to the quadratic solution,

$$\omega_s^2 = \omega_1 \omega_2, \quad (30)$$

which defines the resonance condition for this geometry.

B. 3D micromagnetic simulation

The dynamical susceptibility spectra of the smallest Py disk has been simulated by a micromagnetic code developed by Labbé⁴¹ and later by Boust and Vukadinovic.⁴² In this approach, the disk volume is discretized by a regular cubic mesh of total size $128 \times 128 \times 11$, where each cube has an edge size of 3.9 nm. The magnetization vector is assumed to be uniform inside each cell. This approximation is valid only because the cell size is smaller than the exchange length $\Lambda = 5$ nm for Py. Two 3D codes are used to calculate the dynamical response. For each value of the external field H_{ext} , the first code calculates the stable configuration of the magnetization vector $\mathbf{M}(\mathbf{r})$ by solving the Landau-Lifshitz equation in the time domain. Hence, this code allows one to incorporate in the simulation the small spatial dependence of the direction of \mathbf{M} inside the sample volume in the quasaturated state. The second code computes the full dynamic susceptibility tensor $\hat{\chi}$ from the linearization of the Landau-Lifshitz equation around the local equilibrium configuration. The used material parameters are identical to the ones measured in the extended thin film ($\gamma = 1.849 \times 10^7$ rad s⁻¹ G⁻¹, $4\pi M_s = 9775$ G, $A = 10^{-6}$ erg/cm, and $\alpha = 6 \times 10^{-3}$).

At first, we shall compare the spectra calculated at $\theta_H = 0^\circ$ by the 3D micromagnetic simulation and the 2D analytical model. Figure 12 shows the amplitude of the imaginary part of the simulated susceptibility of the in-plane component χ''_{xx} at four different frequencies: 8.2, 7.0, 5.6, and 4.2 GHz. A series of quantized modes is observed in the 8.2 GHz spectrum. The spatial distribution of the resonant modes in the midplane of the disks are shown in Fig. 13(a) for the three most intense peaks. The observed profiles correspond to the expected eigenmodes $\mathcal{J}_m^\ell(\mathbf{r})$, with $\ell=0$ and $m=0, 1,$

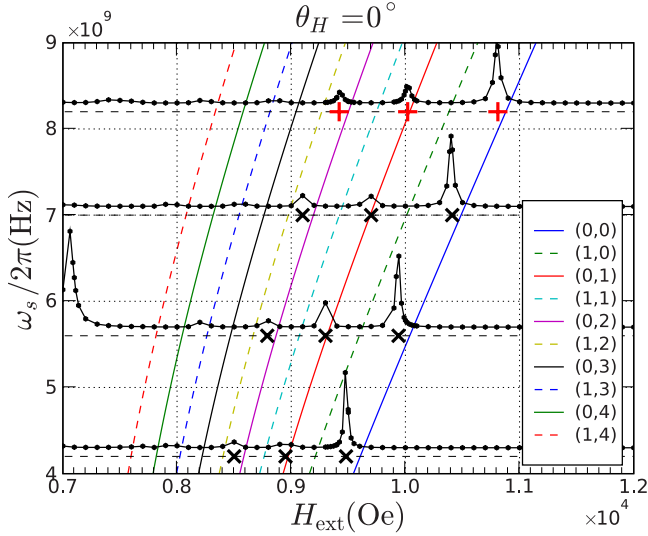


FIG. 12. (Color online) Comparison between the 2D analytical model (oblique lines) and the 3D micromagnetic simulation (horizontal spectra) for the prediction of the resonance fields of a $D_2 = 0.5 \mu\text{m}$ Py disk magnetized at $\theta_H = 0^\circ$. The crosses indicate the positions of the most intense peaks in the simulated spectra. The continuous lines are the locus of the resonance field of the radial modes ($\ell=0, m$) predicted analytically. The dashed lines correspond to the hidden modes ($\ell=1, m$).

and 2, respectively. For comparison we have also plotted in Fig. 12 the locus of the resonances (see oblique lines) predicted by the 2D analytical model using the same parameters as in the 3D model. The agreement between the two models is good for the lowest-energy (highest-field) modes. A small difference of about 120 Oe exists for the lowest-energy mode. The difference must come from the thickness dependency of the precession. Such hypothesis is consistent with the fact that the simulation predicts the resonance slightly higher in energy (lower in field) than the analytical model.

In Fig. 13(b), the calculated transverse susceptibility of the third mode (at $H_{\text{ext}} = 8.8$ kOe) of the 5.6 GHz spectrum is shown along the thickness of the disk. It shows that the magnetization dynamics is not uniform along the thickness, par-

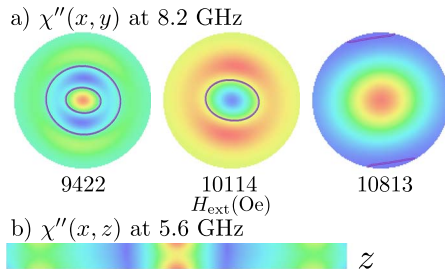


FIG. 13. (Color online) (a) Images of the transverse susceptibility obtained through the 3D micromagnetic simulation for the first three modes (red crosses of Fig. 12) at 8.2 GHz of a $D_2 = 0.5 \mu\text{m}$ Py disk magnetized at $\theta_H = 0^\circ$. The thick lines indicate the nodes of precession. (b) Image of the transverse susceptibility for the third mode (at $H_{\text{ext}} = 8.8$ kOe) of the 5.6 GHz spectrum showing that the magnetization dynamics is not uniform across the thickness of the disk.

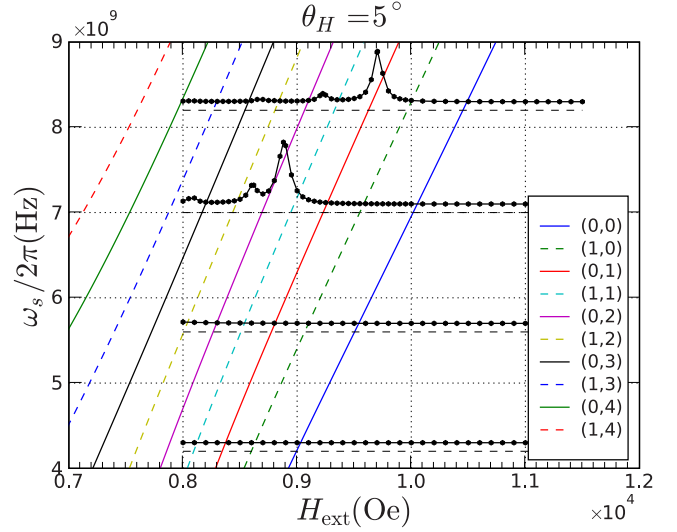


FIG. 14. (Color online) Comparison between the 2D analytical model (oblique lines) and the 3D micromagnetic simulation (horizontal spectra) for the prediction of the resonance fields of a $D_2 = 0.5 \mu\text{m}$ Py disk magnetized at $\theta_H = 5^\circ$. The continuous lines are the locus of the resonance field of the radial modes ($\ell=0, m$) predicted analytically [dashed lines correspond to the hidden modes ($\ell=1, m$)]. The important disagreement between the 3D and 2D models originate from the two simplifications in the analytical model (see text).

ticularly in the center of the disk. This is due to the nonuniformity of the internal field along the thickness, as the disk is magnetized along its normal. This effect would get stronger if the thickness of the disk would be larger and could eventually lead to an edge mode. In fact, the localization of the lowest-energy mode at the top and bottom surfaces of Cu/Py/Cu submicron-size disks, where the thickness of the Py layer was 100 nm, was observed experimentally and calculated by full 3D simulations of χ'' .¹³

We have also performed micromagnetic simulations of the dynamic susceptibility at $\theta_H \neq 0^\circ$, using the same value for the parameters as above. Figure 14 shows the simulated spectrum at $\theta_H = 5^\circ$ for the four same excitation frequencies. The simulations are limited to the quasaturated field range when $H_{\text{ext}} > 8$ kOe. The highest-frequency spectrum at 8.2 GHz shows two resonances. The spatial profile (not shown) of the lowest-energy mode (located at 9.7 kOe on the 8.2 GHz spectrum) resembles $\mathcal{J}_0^0(\mathbf{r})$ described above. Figure 15(a) shows the spatial profile for the second peak at 9.2 kOe on the 8.2 GHz spectrum. The observed spatial profile breaks the axial symmetry due to the small tilt angle that the magnetization makes with the disk normal. This profile can be decomposed in the basis of the normal modes \mathcal{J}_m^ℓ . The results is shown in Fig. 15(b), where we find that

$$\chi''(\mathbf{r}) \approx -\frac{3}{4} \left\{ \frac{1}{3} \mathcal{J}_0^0(\mathbf{r}) - \mathcal{J}_1^0(\mathbf{r}) - \frac{2}{3} \mathcal{J}_0^2(\mathbf{r}) \right\} + \frac{1}{5} \{ \mathcal{J}_2^0(\mathbf{r}) + \mathcal{J}_1^2(\mathbf{r}) + \mathcal{J}_0^4(\mathbf{r}) \}. \quad (31)$$

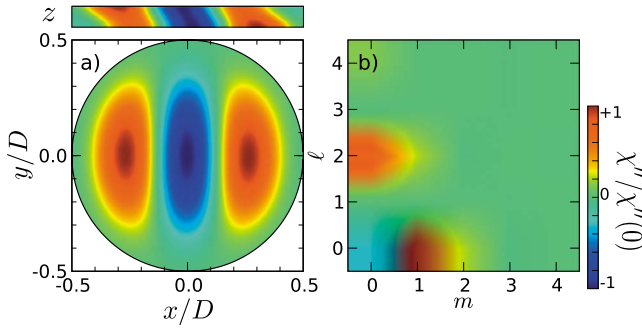


FIG. 15. (Color online) (a) Image of the spatial distribution of the resonant profile for the second peak at 9.2 kOe on the 8.2 GHz simulated spectrum of Fig. 14. The cartography is shown both in the axial and radial middle sections. (b) The mode shown in (a) is now decomposed in the \mathcal{J}_m^ℓ basis. The figure reveals here the spectral weights of the different eigenmodes.

Hence, the normal modes in the presence of a small tilt angle θ_H are no longer the functions \mathcal{J}_m^ℓ but rather a linear combination of them. We have also plotted in Fig. 14 the 2D analytical prediction of the resonance fields as oblique lines. We find an important discrepancy between the two models not only in the location of the resonance for the fundamental mode (almost 850 G apart) but also in the effective gyromagnetic ratio. In order to fit the 3D simulated spectra with the 2D analytical model and θ_H as the adjustable parameter, a much larger value of $\theta_H \approx 10^\circ$ has to be used in the analytical model than in the simulation. This shows the limits of the two main approximations of the 2D model: (i) homogeneous dynamics along the disk thickness and (ii) unperturbed \mathcal{J}_m^ℓ normal-mode basis to compute the resonance fields.

V. COMPARISON WITH THE EXPERIMENTAL DATA

In this section, we want to analyze the three spectroscopic information that are (i) the position, (ii) the amplitude, and (iii) the width of the resonance peaks measured experimentally on the Py disks of thickness 43.3 nm and of diameters $D_1=1.0 \mu\text{m}$ and $D_2=0.5 \mu\text{m}$.

A. Position

As mentioned earlier, the values of the resonance fields are an important indicator of the effective internal field, which should not be disregarded by using the magnetization as a fitting parameter. We shall rely on the value of M_s measured by cavity FMR on the extended thin film used for the fabrication of the disks, and we shall assume that $4\pi M_s = 9775 \text{ G}$ is unchanged after the patterning process. The cavity FMR also provides the value of $\gamma = 1.849 \times 10^7 \text{ rad s}^{-1} \text{ G}^{-1}$ for our alloy composition. We first concentrate on the position of the fundamental mode (highest-field mode) measured on the largest disk, of diameter $D_1 = 1.0 \mu\text{m}$ (see Fig. 9). The blue dots shown in Fig. 16 are the positions of the main peak put in a $(\omega_s, H_{\text{appl}})$ diagram. Also on the figure (red triangle) is the resonance position of the uniform mode measured by the cavity FMR, and the dashed line is the extrapolated locus of the mode as a function of

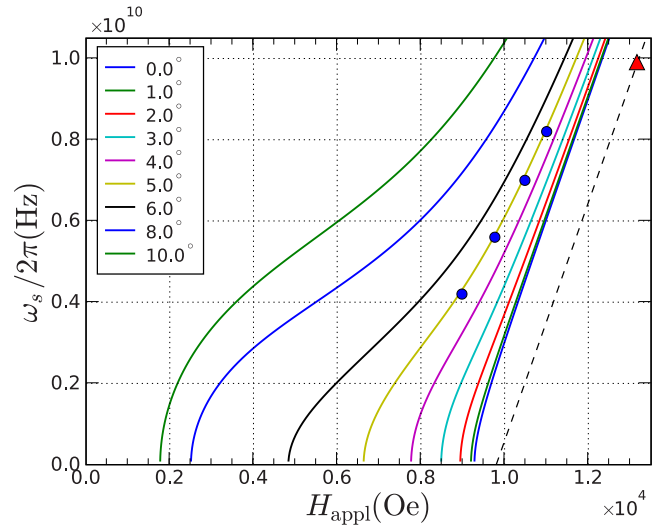


FIG. 16. (Color online) Resonance field of the fundamental mode. Blue dots (see Fig. 9) indicate the measured field on the $D_1=1.0 \mu\text{m}$ disk. Continuous lines are the analytically predicted angle dependence of $H_{\text{res}}(\omega_s)$ for different values of θ_H (lines) with $H_{\text{off}}=-70 \text{ Oe}$. Also indicated is the measured resonance position in the extended film (red triangle). The dashed line represents the asymptote crossing this point and whose slope is the measured gyromagnetic ratio: the shift with the $\theta_H=0^\circ$ line is mainly due to finite-size effects in the disk.

frequency. We use the 2D analytical model presented in Sec. IV A to fit the resonance fields. The results are shown in continuous lines. The two fitting parameters are the angle θ_H and the offset field induced by the tip H_{off} . Because of the way H_{off} is defined in Eq. (9), an additional field to H_{appl} , its adjustment simply corresponds to an over-all shift of the whole set of curves in the $(\omega_s, H_{\text{appl}})$ phase diagram. At $H_{\text{off}}=-70 \text{ Oe}$, the $\theta_H=0^\circ$ line is already shifted by almost 1 kOe lower in field (higher in energy) compared to the extended film. This is due to the cost in exchange and dipolar energies in the nanostructure. Increasing θ_H in Fig. 16 amplifies this shift but it also reduces the effective gyromagnetic ratio γ_{eff} , which becomes frequency dependent. There is a unique value of θ_H that reproduces the experimentally observed frequency dependence of $\gamma_{\text{eff}}(H)$, and the best fit is obtained for $\theta_H=4.9^\circ$. Such a value for θ_H is plausible since our setup does not incorporate a precise goniometer, and the angular orientation is difficult to tune on small size samples. The fit also provides a value for $H_{\text{off}}=-70 \text{ G}$. This value is close to the expected shift induced by the stray field of the tip at the distance $s=3.1 \mu\text{m}$ of the disk.

Using the fit values above, we have reported on Fig. 9 the locus of the higher order modes. The continuous lines indicate the cylindrically symmetric modes ($\ell=0$) and the dashed lines indicates the modes with nonzero angular numbers $\ell \neq 0$, which should be hidden due to the homogeneous excitation field h . We find a good agreement with the data, except at the lowest frequency (4.2 GHz) where a peak appears between the \mathcal{J}_0^0 and \mathcal{J}_1^0 modes. This new resonance is actually close to the location of the \mathcal{J}_1^0 hidden mode. A possible explanation is that this resonance is a reminiscence of the broken-symmetry mode found in the simulation of the

$D_2=0.5 \mu\text{m}$ disk at $\theta_H=5^\circ$. Such a mode, being a combination of mainly \mathcal{J}_0^0 and \mathcal{J}_1^0 , would resonate between the $m=0$ and 1 modes. This mode becomes prominent at the lowest frequency because as the excitation frequency decreases the applied field becomes lower and the magnetic configuration becomes more sensitive to the in-plane component of the applied field, which favors the excitation of a mode having the symmetry of the in-plane component.

The differences between the data and the 2D analytical model can be due to the approximations and assumptions made in the model. One factor that affects the peak position is the value of the pinning condition. The expressions derived above in the 2D approximate model assume a total pinning of the SW at the periphery ($\vartheta_R=0$). Assuming free spins (zero pinning) at the periphery would move the peak position upward in field by about 50 G. It corresponds to keeping the total pinning condition and increasing the disk diameter by some amount of the order of the film thickness.³⁷ Also, the radial component of the stray field of the probe is not taken into account in the model. This would accentuate the effects of θ_H on the static configuration of $\mathbf{M}(\mathbf{r})$ in the sample. Other experimental uncertainties would be sufficient to account for the small discrepancy found in our analysis. We recall that the diameter of the disk used in the model is the one measured by SEM (see Fig. 8). A peripheral oxidation of the alloy cannot be excluded since there is no protective alumina on the periphery of the disks. Change in the disk diameter in the analytical model would shift the resonance peaks and affect the field separations between them. Also, the separation between the probe and the sample and the magnetic moment of the spherical probe are known within 10%. This shows the limits of using the mechanical FMR for a precise determination of the unperturbed FMR peak positions of a submicron-size sample.

Finally we have repeated this analysis on the smaller disk with a diameter of $D_2=0.5 \mu\text{m}$. Fitting the data with the analytical model gives $\theta_H=9.5^\circ$ and $H_{\text{off}}=-760$ Oe. We have reported with straight lines on Fig. 10 the results of the analytical model. The value of θ_H found here is in disagreement with the previous finding, which is somewhat surprising since the two disks are located nearby, on the same substrate. Several arguments suggest that the true value of θ_H is the value for the largest disk, i.e., $\approx 5^\circ$. As shown in Fig. 14, the analytical model tends to underestimate the effect of the angle as the disk shrinks in diameter, compared to the 3D simulation. This affects the shift in the resonance field and the lowering of γ_{eff} , both underestimated by the 2D approximate model. A fit with this model will thus yield to a larger θ_H value than the 3D simulation. If we now compare the experimental results of Fig. 10 with the 3D simulation at $\theta_H=5^\circ$ of Fig. 14, we find that $H_{\text{off}} \approx -1$ kOe, which is a shift larger than the one expected, ≈ -520 Oe from $s=1.0 \mu\text{m}$ (see Sec. II C 2). We emphasize here that the uncertainties mentioned above in the properties of the sample and the probe could translate in substantial errors in the 2D and 3D analytical models. In fact, finite-size effects in the $D_2=0.5 \mu\text{m}$ crucially depend on the exact properties of the sample. Moreover, due to the small separation between the probe and the sample, the effect of the radial stray field from the probe is also more important than for the largest disk.

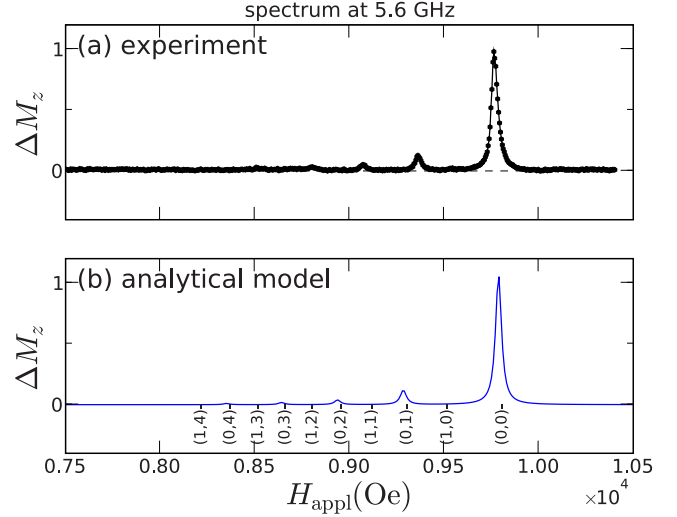


FIG. 17. (Color online) Comparison between experiment and analytical model of the amplitude of the peaks for the disk of diameter $1.0 \mu\text{m}$ at 5.6 GHz.

B. Amplitude

The amplitude of the modes indicates their coupling with the spectrometer. In the following we attempt to predict the relative amplitudes between the peaks. We will concentrate on the 5.6 GHz spectrum measured for the largest disk (cf. Fig. 9).

Since the mechanical FMR is using different schemes for the excitation and detection part, they need to be treated separately. First, we compute the coupling to the excitation, which is identical to all FMR spectrometers. The microwave field being uniform at the scale of the sample, the coupling is simply given by the overlap integral with the transverse susceptibility. In our notation, we find that the angle of precession is given by

$$\vartheta_m = \frac{2h}{\alpha M_s R^2} \int_{r < R} \mathcal{J}_m^0(r) r dr, \quad (32)$$

where we only consider the coupling to the $(\ell=0, m)$ modes and where α is the damping coefficient and h is the amplitude of the microwave field.

Second, the force induced on the cantilever is given by

$$F_{z,m} = m_{\text{sph}} \int_{V_s} \Delta M_{z,m}(\mathbf{r}) \mathcal{G}_{zz}(r, z + s + \Psi/2) d^3r, \quad (33)$$

where the integral is the gradient of field along the z direction induced by the local variation in longitudinal component of magnetization inside the sample, $\Delta M_{z,m}(\mathbf{r}) = \frac{1}{2} M_s \vartheta_m^2 \mathcal{J}_m^\ell(\mathbf{r})^2 / C_{\ell,m}$, and where

$$\mathcal{G}_{zz}(r, z) = \frac{9z}{(r^2 + z^2)^{5/2}} - \frac{15z^3}{(r^2 + z^2)^{7/2}}. \quad (34)$$

In Eq. (33), we have used the fact that our probe has a spherical shape and can be viewed as a magnetic dipole m_{sph} placed at its center.

We have reported in Fig. 17 a comparison between the

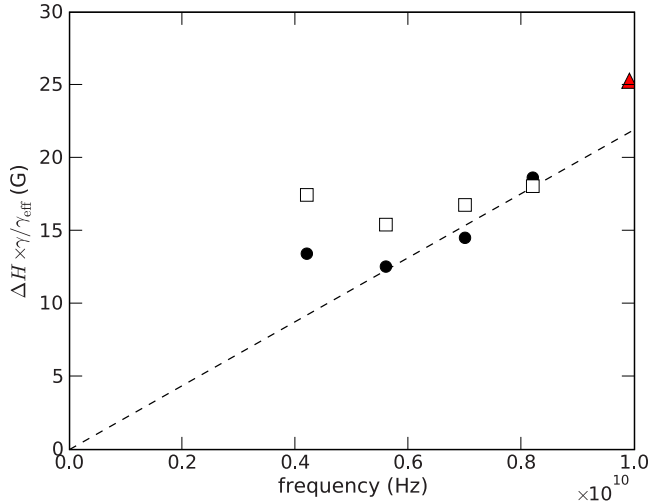


FIG. 18. (Color online) Frequency dependence of the linewidth measured on both the $D_1=1.0 \mu\text{m}$ disk (full circles) and the $D_2=0.5 \mu\text{m}$ disk (open boxes). The red triangle indicates the value measured by cavity FMR on the extended film on Si. The mechanical-FMR data are renormalized by γ_{eff} . The dashed line corresponds to a damping coefficient $\alpha=6 \times 10^{-3}$.

measured spectra and the calculated peak shape using the analytical model and assuming that the linewidth is identical for all the modes. We find a good agreement with the data between the relative height of the peaks. In particular, we observe that the peak amplitude decreases by almost an order of magnitude between the \mathcal{J}_0^0 and \mathcal{J}_1^0 modes. This decrease is less pronounced in conventional FMR which measures the transverse component of the magnetization (see Fig. 12). This implies some caution when comparing the relative amplitude of the peaks found in the 3D simulation of the transverse susceptibility with the one found in the mechanical-FMR experiment.

C. Linewidth

Another important characterization concerns the width ΔH of the resonance line. The full circles and open boxes in Fig. 18 are the linewidths measured as a function of frequency in the Py disks of diameters $D_1=1.0 \mu\text{m}$ and $D_2=0.5 \mu\text{m}$, respectively. All values have been renormalized by the effective gyromagnetic ratio $\gamma_{\text{eff}}=\partial\omega_s/\partial H_{\text{appl}}$. These linewidths are among the smallest reported for Py, confirming the excellent quality of the material used for this study.

The resonance linewidth (half width at midheight of the absorption curve) of the Py polycrystalline magnetic layer is described³⁸ as the sum of two contributions,

$$\Delta H = \frac{1}{2\gamma T_1} + \Delta H^{\text{res}}(\Delta H_u, \Delta \theta_H). \quad (35)$$

The first term relates to the intrinsic relaxation rate of the magnetization vector, whereas the second term corresponds to the inhomogeneous broadening induced by a distribution of internal field, as well as by a distribution of polarization angles, of characteristics widths ΔH_u and $\Delta \theta_H$, respectively. ΔH_u reflects the spatial inhomogeneity of the field parameter

H_u , whereas $\Delta \theta_H$ refers to the distribution of the orientation θ_H of the applied field with respect to the normal to the surface of the individual crystallites.

The results obtained on the disks should be compared to the value observed by cavity-FMR on the extended thin film. In the cavity-FMR studies, the linewidths measured on the film grown on the atomically flat Si substrate in the parallel and in the perpendicular geometries are equal (25 Oe) and reflect almost entirely the homogeneous contribution. The measured value is represented by a red triangle in Fig. 18. It allows for an estimate of the intrinsic damping parameter [$\alpha=1/(2\omega T_1)$], found to be $\alpha=7 \times 10^{-3}$. This value is an upper bound for α since the presence of a small inhomogeneous contribution in the linewidth would reduce the value of the homogeneous part. The film grown on mica presents more inhomogeneities than on Si, the results of which corresponds to a linewidth increase of 3 Oe. This is due to the uneven surface of the mica substrate, which bends over because of the strain between the different sheets of mica.

From the frequency dependence of the linewidth of the large disk, we can estimate the damping coefficient in the nanostructure, found to be $\alpha=6 \times 10^{-3}$ (dashed line on Fig. 18), in good agreement with the upper bound found on the thin film. We find that there is no inhomogeneous broadening in the nanostructure, which means that the small amount observed in the extended film deposited on mica is not relevant in structures confined at the submicron length scale.^{10,13} It also implies that there is no additional broadening induced by the mechanical FMR. Finally, the frequency dependence of the linewidth at low frequencies and of the small disk is not linear. In fact, the magnetization configuration is not uniform at low applied field, and the renormalization of the field linewidths by γ_{eff} is not sufficient to recover the intrinsic behavior. Moreover it was shown on the extended thin film that as the applied field is decreased, the increase in the angle between the equilibrium magnetization and the normal of the film increases the linewidth through the inhomogeneous contribution associated³⁸ to the distribution $\Delta \theta_H$ in Eq. (35).

VI. CONCLUSION

It was shown in this paper how MRFM can be used to detect and *quantitatively* analyze the intrinsic FMR spectra of *individual* submicron-size samples. To realize this objective, the coupling between the magnetic probe attached to the cantilever and the sample has to be optimized. On one hand, it has to be as strong as possible to detect FMR in tiny samples. On the other hand, the inhomogeneity induced by the stray field of the probe has to be small compared to the internal dipolar field inhomogeneity in the sample, in order to detect the intrinsic behavior of the latter. Using a magnetic sphere whose size is of the order of the disk-shaped samples enables us to meet these two requirements. We demonstrate a 1000 spins sensitivity at room temperature. Using two approximate 2D and 3D models, we can understand the measured FMR spectra on Py disks patterned out from the same extended film, whose characteristics are well known. It requires a good understanding of finite-size effects and of the homogeneous shift of the SW modes resonance fields induced by the probe.

Finally, we would like to summarize the main advantages of mechanical FMR: (i) its sensitivity to detect a single magnon excitation in a buried hybrid structure, e.g., below contact electrodes, (ii) its versatility as a near-field technique (i.e., only sensitive to the area directly underneath the probe), which allows spatial imaging of the magnetization dynamics, and (iii) its ability to measure the longitudinal component of the magnetization, a quantity directly linked to the damping.

ACKNOWLEDGMENTS

We are greatly indebted to O. Acher and A.-L. Adenot for their help and support. This research was partially supported by Grant No. ECCS-0653901 from the U.S. National Science Foundation, by ANR under Grant No. PNANO06-0235 from France, and by the European Grant MASTER No. NMP-FP7 212257.

APPENDIX A: DEPOLARIZATION FACTORS OF A CYLINDER

The analytical formula that has been used for the demagnetization tensor, \hat{N} , of a disk of radius R and thickness t are explicitly written in this appendix. The formula were actually derived from the published work of Tandon,⁴³ but we have chosen to reprint them below because a couple of small typographical errors remain in the original paper. The only assumption made here is that the magnetization is homogeneous inside the cylindrical volume.

Because of the axial symmetry, the values of the tensor \hat{N} are better expressed in the cylindrical coordinates (r, z) , and using the notation of Ref. 43, we introduce the reduced units $\zeta = z/R$, $\tau = t/(2R)$, $\rho = r/R$;

$$N_{zz}(r, z) = + \frac{1}{2} \{s_{\zeta, \tau} I_0(\rho, \alpha_-) + I_0(\rho, \alpha_+)\}, \quad (\text{A1a})$$

$$N_{zz}(r, z) = - \frac{1}{2} \{I_1(\rho, \alpha_-) - I_1(\rho, \alpha_+)\}, \quad (\text{A1b})$$

$$\begin{aligned} N_{rr}(r, z) = & + \frac{1}{4} \{s_{\zeta, \tau} I_2(\rho, \alpha_-) + I_2(\rho, \alpha_+) - 2H_{\tau, \zeta} I_2(\rho, 0)\} \\ & - \frac{1}{4} \{s_{\zeta, \tau} I_0(\rho, \alpha_-) + I_0(\rho, \alpha_+) - 2H_{\tau, \zeta} I_0(\rho, 0)\}, \end{aligned} \quad (\text{A1c})$$

where the notations $\alpha_- = |\zeta - \tau|$ and $\alpha_+ = |\zeta + \tau|$ are, respectively, the distance (in reduced units) with the bottom and top surface of the cylinder. The function s and H design, respectively, the Sign and Heaviside functions,

$$s_{x,y} = \begin{cases} +1 & \text{if } x < y \\ -1 & \text{else,} \end{cases}$$

$$H_{x,y} = \begin{cases} 1 & \text{if } x > y \\ 0 & \text{else.} \end{cases}$$

The integrals I_i have the following expressions:

$$I_0(\rho, \alpha) = s_{1, \rho} \frac{1}{2} \Lambda_0(\beta, \kappa) - \frac{k\alpha}{2\pi\sqrt{\rho}} K(k) + H_{1, \rho}, \quad (\text{A2a})$$

$$I_1(\rho, \alpha) = \frac{1}{\pi k \sqrt{\rho}} \{(2-m)K(k) - 2E(k)\}, \quad (\text{A2b})$$

$$\begin{aligned} I_2(\rho, \alpha) = & \frac{2\alpha}{\pi k \rho^{3/2}} E(k) - (\alpha^2 + \rho^2 + 2) \frac{\alpha k}{2\pi \rho^{5/2}} K(k) \\ & - s_{1, \rho} \frac{1}{2\rho^2} \Lambda_0(\beta, \kappa) + \frac{H_{1, \rho}}{\rho^2}, \end{aligned} \quad (\text{A2c})$$

where

$$m = k^2 = \sin^2 \kappa = \frac{4\rho}{(\rho+1)^2 + \alpha^2}, \quad (\text{A3a})$$

$$\beta = \arcsin\left(\frac{\alpha}{\sqrt{(\rho-1)^2 + \alpha^2}}\right), \quad (\text{A3b})$$

where $K(k)$ and $E(k)$ are the complete elliptic integrals of the first and second kind and Λ_0 is the Heuman's lambda function.

The above expressions are valid everywhere in space. The magnetic-field induction at every point in space (inside or outside the sample's volume) simply obeys the formula,

$$B_z(r, z) = H_{\text{ext}} + 4\pi M_s \{\Theta(r, z) - N_{zz}(r, z)\}, \quad (\text{A4})$$

where Θ is a function equals to 1 inside the cylindrical volume and 0 otherwise,

$$\Theta(r, z)_{x,y} = \begin{cases} 1 & \text{if } r < R \text{ and } |z| < t/2 \\ 0 & \text{else.} \end{cases}$$

APPENDIX B: LINEARIZATION IN THE LOCAL FRAME

The notations have been defined in Fig. 11: (x, y, z) is the Cartesian frame along the principal axis of the disk with z oriented along the normal and (ξ, y, ζ) the Cartesian frame of the magnetization dynamics with ζ along the equilibrium (or effective magnetic field) direction. Both frames are related by a rotation of an angle θ around the y direction. If θ_H is the angle that the external magnetic field makes with the normal of the disk, then θ is implicitly defined by the equilibrium condition,

$$H_{\text{ext}} \sin(\theta - \theta_H) + 2\pi M_s \overline{N_{xx}} \sin 2\theta - 2\pi M_s \overline{N_{zz}} \sin 2\theta = 0. \quad (\text{B1})$$

In all the expressions above, the tensors are expressed in the Cartesian frame of the disk (x, y, z) . This applies for the demagnetizing factors \hat{N} in Appendix A but also for the matrices,

$$\mathbf{zz} = \begin{bmatrix} 0 & 0 & 0 \\ 0 & 0 & 0 \\ 0 & 0 & 1 \end{bmatrix}, \quad (\text{B2})$$

$$\mathbf{x}\mathbf{x} = \begin{bmatrix} 1 & 0 & 0 \\ 0 & 0 & 0 \\ 0 & 0 & 0 \end{bmatrix}. \quad (\text{B3})$$

Solving Eq. (24) requires us to write down the different tensors $\hat{\mathbf{T}}(=\hat{\mathbf{N}},\hat{\mathbf{G}})$ in the local frame of the magnetization. This is achieved through the transformation $\hat{\mathcal{R}}_\theta^t \hat{\mathbf{T}} \hat{\mathcal{R}}_\theta$, where $\hat{\mathcal{R}}_\theta$ is the rotation matrix between the (x,y,z) and (ξ,y,ζ) ,

$$\hat{\mathcal{R}}_\theta = \begin{bmatrix} \cos \theta & 0 & -\sin \theta \\ 0 & 1 & 0 \\ \sin \theta & 0 & \cos \theta \end{bmatrix}, \quad (\text{B4})$$

and the subscript t stands for the transpose.

This allows us to find the expression Eq. (29), where we have used symmetry arguments to impose $\overline{N_{xy}} = \overline{N_{xz}} = 0$.

*Corresponding author. olivier.klein@cea.fr

¹H. Stoll *et al.*, Appl. Phys. Lett. **84**, 3328 (2004).

²Y. Acremann, J. P. Strachan, V. Chembrolu, S. D. Andrews, T. Tylliszczak, J. A. Katine, M. J. Carey, B. M. Clemens, H. C. Siegmann, and J. Stohr, Phys. Rev. Lett. **96**, 217202 (2006).

³J. Vogel, W. Kuch, M. Bonfim, J. Camarero, Y. Pennec, F. Offi, K. Fukumoto, J. Kirschner, A. Fontaine, and S. Pizzini, Appl. Phys. Lett. **82**, 2299 (2003).

⁴K. Perzlmaier, M. Buess, C. H. Back, V. E. Demidov, B. Hillebrands, and S. O. Demokritov, Phys. Rev. Lett. **94**, 057202 (2005).

⁵W. K. Hiebert, A. Stankiewicz, and M. R. Freeman, Phys. Rev. Lett. **79**, 1134 (1997).

⁶A. Barman, V. V. Kruglyak, R. J. Hicken, A. Kundrotaite, and M. Rahman, Appl. Phys. Lett. **82**, 3065 (2003).

⁷M. Buess, R. Höllinger, T. Haug, K. Perzlmaier, U. Krey, D. Pescia, M. R. Scheinfein, D. Weiss, and C. H. Back, Phys. Rev. Lett. **93**, 077207 (2004).

⁸A. A. Tulapurkar, Y. Suzuki, A. Fukushima, H. Kubota, H. Maehara, K. Tsunekawa, D. D. Djayaprawira, N. Watanabe, and S. Yuasa, Nature (London) **438**, 339 (2005).

⁹J. C. Sankey, P. M. Braganca, A. G. F. Garcia, I. N. Krivorotov, R. A. Buhrman, and D. C. Ralph, Phys. Rev. Lett. **96**, 227601 (2006).

¹⁰W. Chen, J.-M. L. Beaujour, G. de Loubens, A. D. Kent, and J. Z. Sun, Appl. Phys. Lett. **92**, 012507 (2008).

¹¹Z. Zhang, P. C. Hammel, and P. E. Wigen, Appl. Phys. Lett. **68**, 2005 (1996).

¹²V. Charbois, V. V. Naletov, J. B. Youssef, and O. Klein, Appl. Phys. Lett. **80**, 4795 (2002).

¹³G. de Loubens, V. V. Naletov, O. Klein, J. B. Youssef, F. Boust, and N. Vukadinovic, Phys. Rev. Lett. **98**, 127601 (2007).

¹⁴K. Wago, D. Botkin, C. S. Yannoni, and D. Rugar, Appl. Phys. Lett. **72**, 2757 (1998).

¹⁵E. Nazaretski, I. Martin, R. Movshovich, D. V. Pelekhov, P. C. Hammel, M. Zalalutdinov, J. W. Baldwin, B. Houston, and T. Mewes, Appl. Phys. Lett. **90**, 234105 (2007).

¹⁶C. Herring and C. Kittel, Phys. Rev. **81**, 869 (1951).

¹⁷M. Bailleul, R. Hollinger, and C. Fermon, Phys. Rev. B **73**, 104424 (2006).

¹⁸P. E. Wigen, Thin Solid Films **114**, 135 (1984).

¹⁹O. Klein, S. Donovan, M. Dressel, and G. Grüner, Int. J. Infrared Millim. Waves **14**, 2423 (1993).

²⁰S. Donovan, O. Klein, M. Dressel, K. Holczer, and G. Grüner, Int. J. Infrared Millim. Waves **14**, 2459 (1993).

²¹D. Rugar, R. Budakian, H. J. Mamin, and B. W. Chui, Nature (London) **430**, 329 (2004).

²²H. J. Mamin, M. Poggio, C. L. Degen, and D. Rugar, Nat. Nanotechnol. **2**, 301 (2007).

²³H. Suhl, J. Phys. Chem. Solids **1**, 209 (1957).

²⁴G. de Loubens, V. V. Naletov, and O. Klein, Phys. Rev. B **71**, 180411(R) (2005).

²⁵O. Klein, V. Charbois, V. V. Naletov, and C. Fermon, Phys. Rev. B **67**, 220407(R) (2003).

²⁶J. A. Sidles, J. L. Garbini, K. J. Bruland, D. Rugar, O. Züger, S. Hoen, and C. S. Yannoni, Rev. Mod. Phys. **67**, 249 (1995).

²⁷Y. Obukhov *et al.*, Phys. Rev. Lett. **100**, 197601 (2008).

²⁸K. Holczer, O. Klein, and G. Grüner, Solid State Commun. **78**, 875 (1991).

²⁹H. J. Mamin and D. Rugar, Appl. Phys. Lett. **79**, 3358 (2001).

³⁰O. Klein and V. V. Naletov, C. R. Phys. **5**, 325 (2004).

³¹G. de Loubens, Ph.D. thesis, Université Paris XI, 2005.

³²R. Urban, A. Putilin, P. E. Wigen, S.-H. Liou, M. C. Cross, P. C. Hammel, and M. L. Roukes, Phys. Rev. B **73**, 212410 (2006).

³³N. Bloembergen and S. Wang, Phys. Rev. **93**, 72 (1954).

³⁴R. W. Damon and J. R. Eshbach, J. Phys. Chem. Solids **19**, 308 (1961).

³⁵B. A. Kalinikos and A. N. Slavin, J. Phys. C **19**, 7013 (1986).

³⁶G. N. Kakazei, P. E. Wigen, K. Y. Guslienko, V. Novosad, A. N. Slavin, V. O. Golub, N. A. Lesnik, and Y. Otani, Appl. Phys. Lett. **85**, 443 (2004).

³⁷K. Y. Guslienko, S. O. Demokritov, B. Hillebrands, and A. N. Slavin, Phys. Rev. B **66**, 132402 (2002).

³⁸H. Hurdequint, J. Magn. Magn. Mater. **242-245**, 521 (2002).

³⁹H. Hurdequint, J. Magn. Magn. Mater. **310**, 2061 (2007).

⁴⁰S. Mizukami, Y. Ando, and T. Miyazaki, J. Magn. Magn. Mater. **226**, 1640 (2001).

⁴¹S. Labbé and P.-Y. Bertin, J. Magn. Magn. Mater. **206**, 93 (1999).

⁴²F. Boust and N. Vukadinovic, Phys. Rev. B **70**, 172408 (2004).

⁴³S. Tandon, M. Beleggia, Y. Zhu, and M. De Graef, J. Magn. Magn. Mater. **271**, 9 (2004).